Sintering of Ceramic Materials Under Electric Field

Kiran S. Naik

Advisor: Prof. Vincenzo M. Sglavo
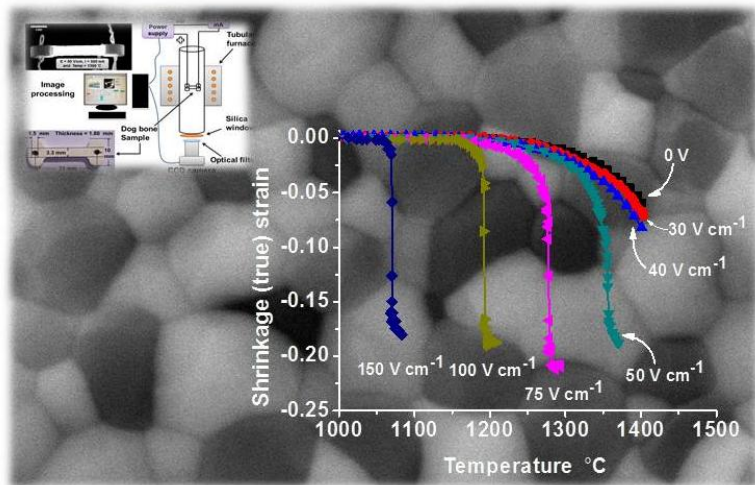
June 2014

Sintering of Ceramic Materials Under Electric Field

Kiran Suresh Naik

E-mail: naik.kiran@ing.unitn.it

Approved by:

Prof. Vincenzo Maria Sglavo,
Advisor
Department of Industrial
Engineering
University of Trento, Italy.

Ph.D. Commission:

Prof. Vincenzo Maria Sglavo,
Department of Industrial
Engineering
University of Trento, Italy.

Prof. Rajesh Prasad,
Department of Applied
Mechanics
*Indian Institute of Technology
New Delhi, India.*

Prof. Lorella Ceschini,
Department of Industrial
Engineering
Alma Mater Studiorum
University of Bologna, Italy.

University of Trento,

Department of Materials Science and Engineering

June 2014

To my family

Abstract

The remarkable discovery of flash sintering came across during the early work of Cologna *et al.* and emerged as an attractive technique in the field of ceramic processing. In this technique the applied electric field initiates the "flash" event, while the densification is controlled by the current density set. Sintering occurs in less than 5 s at a threshold temperature for a given applied field.

The objective of this thesis is to analyse the phenomena of flash sintering with different ceramic oxides; such as alumina-zirconia composite, hydroxyapatite and doped-alumina. The technique involved the application of constant electric field to a dog bone shaped specimen by means of two platinum electrodes while heating. Experiments were performed either in constant heating rate or in Isothermal condition.

For the two-phase 3YSZ-alumina ceramic flash sintering was studied by constant heating rate (CHR) and isothermal sintering experiments. In CHR experiment the 50 vol% 3YSZ-alumina composite was shown to flash sinter at a furnace temperature of 1060°C under an electrical field of 150 V cm^{-1}. Conversely, undoped single-phase alumina remains immune to sintering under fields up to 1000 V cm^{-1}, although single-phase 3YSZ flash sinters at 750°C (furnace temperature). The mechanisms of field assisted sintering are divided into two regimes. At low fields the sintering rate increases gradually (FAST), while at high fields sintering occurs abruptly (FLASH). Interestingly, alumina/zirconia composites show a hybrid behaviour such that early sintering occurs in FAST mode, which is then followed by flash-sintering. The specimens held in the flashed state, after they had sintered to nearly full density, show much higher rate of grain growth than in conventional experiments. These results are in con-

trast to earlier work where the rate of grain growth had been shown to be slower under weak electrical fields.

In the case of isothermal field-assisted sintering of two-phase, 50 vol% 3YSZ-alumina, the composites exhibit an incubation time for the onset of the flash event. Weaker applied fields and lower temperatures lengthen the incubation period. The effect is highly non-linear. For example at 1300°C and 150 V cm^{-1} the flash occurs nearly instanteously (in 10 s), but extends to two hours at 1275°C and 65 V cm^{-1}. This behaviour is reminiscent of nucleation and growth phenomena in chemically driven experiments involving phase transformations in the solid state. Here, a model for nucleation under electrical driving forces, based upon the growth of embryos of colossal permittivity is presented.

The flash sintering was also studied for composites with increasing volume faction of alumina in zirconia (10-50 vol%). The flash onset temperature or the incubation time for the 3YSZ-alumina composites increases with increasing the alumina volume fraction.

In case of CHR experiments of hydroxyapatite, flash effect was shown at 840°C for an applied field of 2000 V cm^{-1}. All the flash sintered samples show stable hydroxyapatite phase. However the sample sintered at 500 V cm^{-1} requires higher sintering temperature and shows enhanced preferred orientation due to higher diffusivity along c-axis.

In case of alumina, field in excess to 1000 V cm^{-1} are required to induce flash effect, whereas doped alumina shows flash sintering at 1000 V cm^{-1}.

Table of Contents

Chapter 1
Introduction

Ceramics are classified as inorganic and non-metallic materials that are essential to our everyday life. They include materials that are weak and strong; friable and tough; opaque and transparent; insulator, conductor, and semiconductor; high melting and low melting; single crystal, polycrystalline, and composite; and so on. The manufacturing and use of ceramics began about 7000 BC [1]. In general, ceramic fabrication requires three main successive steps, first and foremost the synthesis. There are many different methods in order to synthesise powder, like solid state synthesis, sol-gel method, hydrothermal method etc. The second step is to shape the powder into required shape, also called as green sample; and the third, most important is the final step called as sintering.

Sintering involves high temperature treatment of the green sample at a temperature little lower than the melting point of ceramics. It leads to dense ceramics with very less porosity. During the sintering treatment, several phenomena provide the driving force for consolidation and densification. These could cause some effect on grain growth, phase stability, etc. Therefore the final properties of ceramics strongly depend on the sintering process. The sintering can be classified depending on the driving force acting on it. Some of the most common techniques are solid state sintering, pressure assisted sintering and field assisted sintering; which are discussed in detail in the next chapter.

In 2010 Cologna et al. introduced a new field assisted sintering technique, where densification occurs in few seconds called as flash sintering [2]. The flash sintering process gains more attention in the processing of ceramic oxides, due to its high sintering rate and low energy consumption.

The present work sets out to investigate the flash phenomenon in three different ceramic oxides: alumina-zirconia composite, hydroxyapatite, and alumina (doped and un-doped alumina). The flash experiments, prior to this thesis, were conducted only on single phase or doped ceramics oxides. Among various flash sintered ceramics, yttria stabilized zirconia was the widely studied ceramic oxide to understand the mechanisms involved during flash sintering [2–7] Studies on pure and MgO-doped alumina suggest a role for grain boundary conductivity. Whereas pure alumina remains inert to the applied field, the addition of MgO, which is known to promote conventional sintering by segregating to grain boundaries,[8] instills flash sintering in alumina [9].

Both, alumina and 3YSZ known to have different electrical properties; the 3YSZ act as ionic conductor and Al_2O_3 is known for its insulating behavior. The solubility of alumina in zirconia is very low: that is at 1700°C the solubility of 8YSZ in alumina was 0.5-0.8 mol% [10], approx. 0.7 mol% when sintered at 1650°C [11] and is around 1wt% when sintered at 1500°C [12]. Sintering with different volume ratio of Al_2O_3 and zirconia was found to modify its microstructural, electrical and mechanical properties [13–17]. From this knowledge, equal volume composite constituted from alumina and yttria stabilized zirconia was studied using electric field assisted technique. To our knowledge this is the first study of flash sintering in two-phase ceramics. The DC electric field was employed in two-electrode experiments to obtain densification of these composites at low furnace tempera-

2

tures. The results are compared to conventional sintering. Similarly the role of alumina in flash sintering of composite is also investigated.

The second oxide studied by field assisted sintering is hydroxyapatite (HA). HA is one of the most commonly used bio ceramics for biomedical applications such as bone implantation due to its structural similarities with bone tissue resulting in a superior biocompatibility [18–21] . HA ceramics facilitate the new bone formation after implantation and increase the osteoconductive properties. HA can be synthesized by different processes; however for the implantation application it requires to be in dense form. The densification is usually achieved by sintering. In order to obtain highly dense HA the sintering process has to be carried out at high temperatures with longer holding time. Such sintering treatment can therefore have various effects such as; alter the microstructural properties like grain size, leads to phase instability and undesirable chemical reactions. These alterations can in turn have a negative impact on properties like bioactivity and mechanical strength of HA [22].

In order to overcome the above mentioned negative impacts researchers have recently shown interest in reducing the sintering temperature and time in order to obtain dense HA with high mechanical strength and desired microstructure while preventing the phase transformation. Furthermore, the energy and thus the cost associated with the process is also reduced by decreasing the sintering temperature and time. Traditional methods for enhancing sintering rates and lower the sintering temperatures include pressure assisted methods such as hot pressing [23,24], hot isostatic pressing [25], sinter forging and liquid phase sintering. Another approach is the use of Field Assisted Sintering Techniques (FAST) such as microwave sintering [26,27] and spark plasma sintering (SPS) and flash sintering. These methods involve application of different electro-magnetic fields [28,29].

3

The third oxide studied by electric field assisted sintering is alumina. Flash sintering of 0.25 wt% MgO doped alumina was known to occurs at 1000 V cm^{-1}, while undoped alumina remains unaffected for the same applied field [9]. Electric field higher than 1000 V cm^{-1} was applied to un-doped alumina, in order to observe if applied field in excess to 1000 V cm^{-1} can influence flash sintering. The flash sintering behaviour of MgO-doped and Fe_2O_3 doped alumina is compared at applied field of 1000 V cm^{-1} for two different dopant concentration.

The structure of this thesis is as following. In chapter 2, a short overview of sintering and some field assisted sintering techniques have been discussed. The flash sintering technique is briefly described with the help of the reported results, which provide basic understanding and are helpful for further discussions on flash sintering. Chapter 3 provides the experimental method and procedure used for this study. Chapter 4 is divided into five sections. Each section demonstrates a new experimental technique. The first three sections discuss the results on alumina zirconia composite. The fourth section demonstrates the results on hydroxyapatite. The fifth section describes the results on pure and doped alumina. Chapter 5 describes the novel conclusions form the chapter 4. The present thesis demonstrates the flash sintering approach with original results and some new findings to explain these results.

Chapter 2
Literature review

For ceramics processing, different methods have been mentioned in the literature. In this chapter we will discuss some useful sintering techniques to build up a scenario for flash sintering.

2.1 Sintering

Sintering is a processing technique used to produce density-controlled materials from powders by applying thermal energy. Sintering can be achieved by heating the green sample or powder compact to a temperature 2/3 of its melting point [30,31].

2.1.1 Driving force for sintering

Sintering always occurs by lowering the free energy of the system. The sources which lower the free energy provide the driving forces for sintering. The possible driving forces for sintering are [32]:

a) The curvature of the particle surface
b) An externally applied pressure
c) Chemical reaction

In the absence of an external applied pressure and chemical reaction, the decrease in surface free energy (E_s) of the system for spherical particles with radius a is given as:

$$E_s = \frac{3\gamma_{SV}V_m}{a} \quad (1)$$

where γ_{SV} is the specific surface energy of the particle and V_m is the molar volume. The decrease in surface energy is inversely proportional to the radius of the particles.

2.1.2 Matter transport

The driving force initiate the sintering, but actual sintering requires transport of matter. In crystalline solids sintering occurs by diffusion process involving atoms, ions, or molecules [32]. The presence of defect in the crystal will allow diffusional mass transport to take place. In general, defect can be classified into three groups: point defects (Vacancies, interstitial atom and substitutional atoms), line defects (dislocations) and planar defects (free surfaces, grain boundaries, and crystallographic shear planes). Mass transport and also electrical properties of ceramics are mostly determined by the number and type of point defects. Most of our discussion will be confined to point defects in ceramics.

2.1.3 Mechanisms of sintering

As described above, the driving force for sintering of particles provides the path for diffusional transport of matter. However, the matter transport along definite paths defines the mechanisms of sintering. Looking at the assembly of three particles (Fig. 2), there are six different mechanisms of sintering which are represented by numbers in the figure below. The mechanisms are based on matter transport from source to the sink. The source of the matter transport determines the six different mechanisms, since the sink for diffusion is always the neck of the particle. The neck of the particle has cer-

tainly much lower energy and thus always will be the sink for the mass transport. Different mechanisms characterised by the source and the sink are described in table. 1. Only some of these mechanisms as indicated in the table contribute for densification.
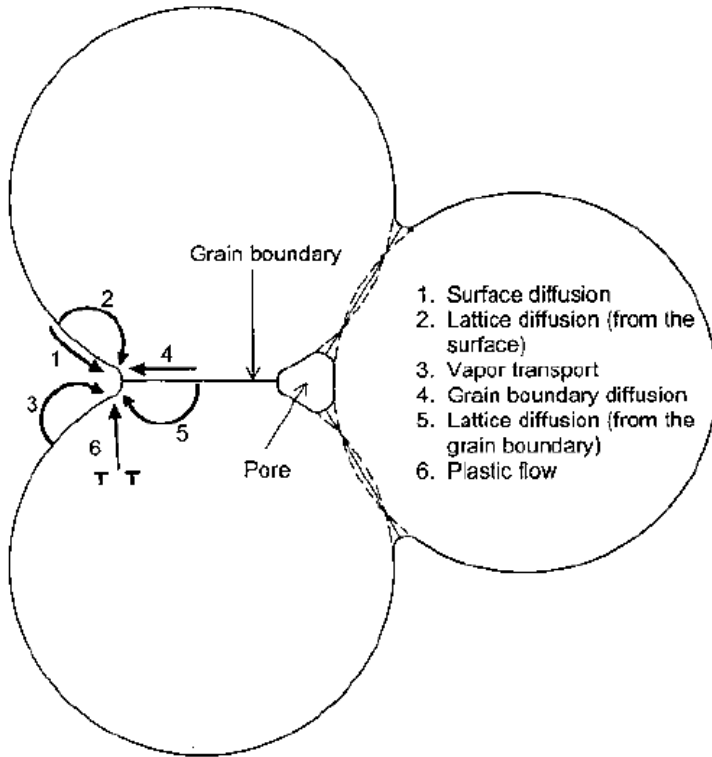
Fig. 1 Material transport paths during sintering [32]

Table 1. Mechanism of Sintering in Polycrystalline Solids [32]

Mechanism	Source of Matter	Sink of Matter	Densifying
1. Surface diffusion	Surface	Neck	X
2. Lattice diffusion	Surface	Neck	X
3. Vapor transport	Surface	Neck	X
4. Grain boundary diffusion	Grain boundary	Neck	√
5. Lattice diffusion	Grain boundary	Neck	√
6. Plastic flow	Dislocations	Neck	√

2.1.4 Stages of sintering

The general process of solid state sintering is normally known to occur in three different stages- initial, intermediate and final. Fig. 11 schematically depicts the densification curve along with the microstructure during each stage of sintering.

Stage I (Initial stage): The initial stage consists of rapid interparticle neck growth by diffusion, vapour transport, plastic flow or viscous flow. The driving force during the initial stage is the large difference in surface curvature of the particles. Densification is accompanied by neck growth for the densifying mechanisms (see table 1). For a powder system this corresponds to a linear shrinkage of 3%-5%, or an increase in relative density of approx. 0.65 when the densifying mechanisms dominate.

Stage II (Intermediate stage): Once the necks are formed between the particles, pores form interconnected channels along the three grain edges. As sintering proceeds, the pore channels get disconnected and form isolated pores because of surface and interfacial tension. Densification is assumed to occur by the pore shrinking to reduce their cross-section and at the same time the grains grow. This is the beginning of final stage of densification. The intermediate stage covers the major part of sintering process and ends when the density is approx. 0.90 of the theoretical.

Stage III (Final stage): The final stage begins when pores pinch off and become isolated at the grain corners [33]. The pores are assumed to shrink continuously to zero size in stable fashion. The relative density obtained in the final stage is always > 0.90 of the theoretical.
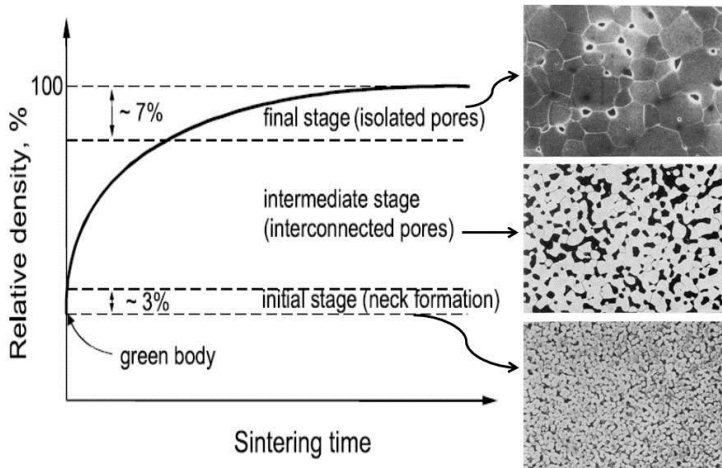

Fig. 2. Schematic representation of the densification curve of a powder compact and the three stages of sintering [32][34].

9

2.2 Types of sintering

2.2.1 Pressure Assisted sintering

Sintering is also enhanced by externally applied pressure in order to obtained sufficient densification. The sintering techniques involving external pressure are hot pressing, hot isostatic pressing and sinter forging or hot forging. Among the three techniques hot pressing is the most widely used technique to provide dense ceramics. The main advantage of pressure assisted sintering is the ability to enhance densification rate relative to coarsening (that is high density and fine grain size). The technique can be also useful for highly covalent bonded ceramics and for ceramic matrix composites.

2.2.1.1 Hot Pressing

In hot pressing, heat and pressure are applied to a sample in the form of powder or a green compact, in a die (Fig.4a). Graphite is the most commonly used die material because of its low cost, ease of machinability and excellent creep resistance at high temperature. However, use of graphite has its own common problems such as its oxidation and chemical reactivity with the samples, which limits it's used during hot pressing. The technique uses operating pressures ranging from $\sim$ 10 to $\sim$ 75 MPa and operating temperature up to 2000°C or higher, depending on the material to be sintered.

2.2.1.2 Hot Isostatic pressing (HIP)

In HIP the pre-consolidated powder is first enclosed in a glass or metal container that is sealed under a vacuum and then placed in a pressure vessel. Alternatively, the sample is first densified

till close porosity, prior to HIP. The external pressure is applied by compressing inert gas (Fig.4c). HIP systems designed for inert gases can routinely be operated at temperature up to ～ 2000 °C and pressures up to ～ 200 MPa (30,000 psi).

2.2.1.3 Sinter-forging (hot forging)

The technique is similar to that of hot pressing except no die is used in sinter forging. In this technique a partially sintered sample is heated with applied uniaxial stress which provides additional driving force for sintering (Fig. 4b).
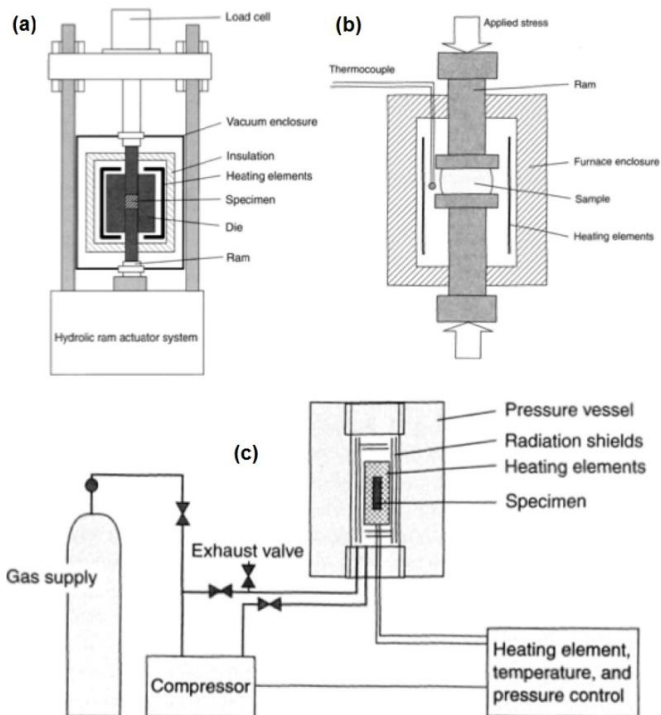
Fig. 3 Schematic for pressure assisted sintering (a) Hot Pressing, (b) Sinter-forging, and (c) Hot Isostatic pressing

2.2.2 Field assisted sintering

2.2.2.1 Microwave Assisted Sintering

Just as application of pressure can enhance sintering, application of field such as electromagnetic radiation can also enhance sintering depending upon the response of the specimen toward the applied field.

Microwave heating is fundamentally different compared to conventional heating. Use of microwaves allows transfer of energy directly into the materials, where it is converted to heat through absorption mechanisms such as ionic conduction, dipole relaxation, and photon-phonon interaction. Thus, microwave-sintering techniques allow a volumetric heating, which in turn allows application of high heat-up rates, markedly shortening the processing time and overcoming difficulties of conventional fast firing technique. The sketch of heating pattern in conventional as well as in microwave sintering is shown in figure 4. Microwave lies in the electromagnetic radiation band in the wavelength range from 1 mm to 1m in free space with frequency between 300 GHz to 300 MHz, respectively.

The technique in microwave sintering is quite simple, the sample to be sintered is placed into the cavity and microwave radiation is applied to the specimen which initiates the process of densification in much faster rate compared to conventional sintering.
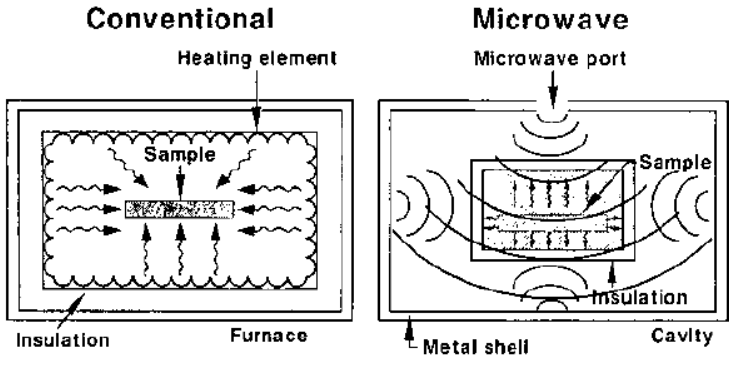
Fig. 4. heating process in conventional and microwave sintering [32].

2.2.2.2 Spark Plasma Sintering

The second most widely used field assisted technique is Spark Plasma Sintering (SPS) [35–38]. The technique involves the consolidation of power under the action of electric field and a uniaxial pressure. The applied current causes Joule heating which differentiates this technique from hot pressing technique. Typical experimental setup used for SPS is shown in Fig. 5. The sample (powder) is loaded into a graphite die and placed into the chamber. The electrodes force current through the graphite die and pressure is applied simultaneously. The most attractive features of SPS process is the enhanced densification with fine grained microstructure.
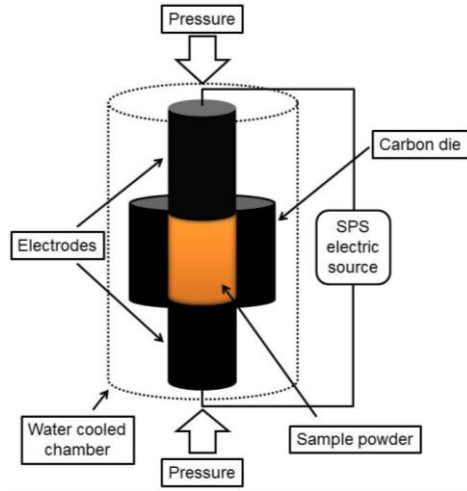
Figure 5 Schematic of Spark Plasma Sintering (SPS) apparatus.

2.2.2.3 Flash Sintering

The initial experiments of flash sintering was introduced by Cologne et al. [2] at University of Colorado at Boulder on 3 mol% Yttria Stabilized Zirconia (3YSZ). 3YSZ requires temperature of around 1400°C or more for full densification by conventional sintering. However when flash sintering was carried out on 3YSZ the sintering rate was significantly enhanced and the required sintering temperature was reduced. It was shown that sintering of 3YSZ can occurs in few seconds to its full density at 120 V cm^{-1} at a furnace temperature of 850°C. In this technique a constant voltage was applied to heating dog bone specimen by means platinum electrode. The furnace heated at a constant heating rate of 10 °C min^{-1}.

A typical specimen response during electric field assisted sintering of 3YSZ as demonstrated by Cologna et al. is shown in Fig.6. The field assisted sintering is characterized by two types of

14

curves, at low electric fields (< 45 V cm^{-1}) by FAST sintering behavior, whereas for electric fields > 45 V cm^{-1} showing flash sintering with vertical sintering curves.
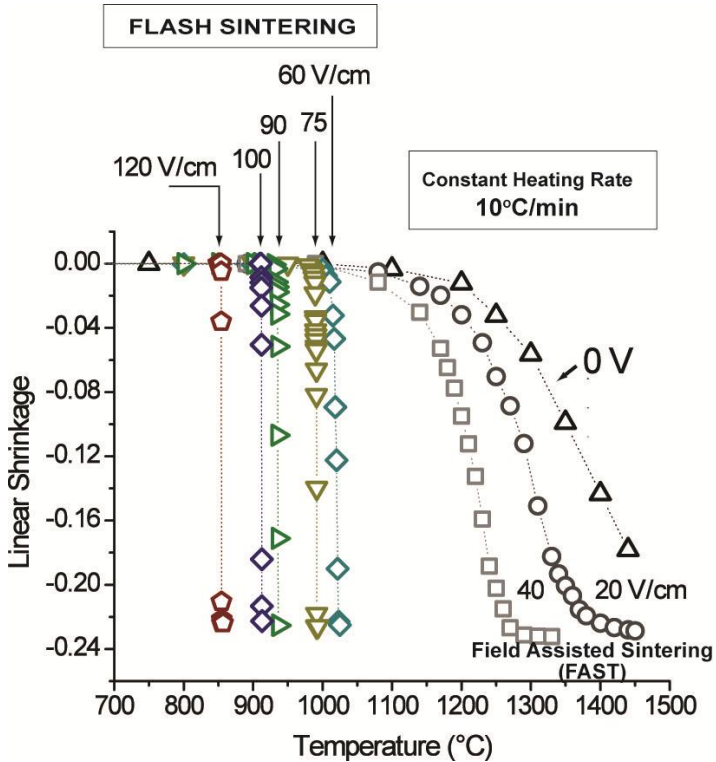
Fig 6. Flash sintering of 3 mole% yttria stabilized zirconia (3YSZ) [2].

The technique was also extended on other ceramic oxides. In case of 8YSZ, 30 V cm^{-1} is sufficient to induce flash due to the higher conductivity of 8YSZ than 3YSZ. In highly conducting samples flash sintering is even possible at 5 V cm^{-1} [39–41]. The sintering is also shown less than 100 °C (furnace temperature) in case of La$_{0.6}$Sr$_{0.4}$Co$_{0.2}$Fe$_{0.8}$O$_3$ [41]. As the conductivity of the ceramic de-

15

creases, required voltage to induce flash sintering is much higher or occurs at higher temperature. Alumina (MgO doped) which is insulating requires applied field of 500 V cm^{-1} to induce flash effect. The required furnace temperature as a function of applied electric field for flash sintering of most of the ceramic oxides is shown in Fig. 7 [2,3,9,39,42–45].
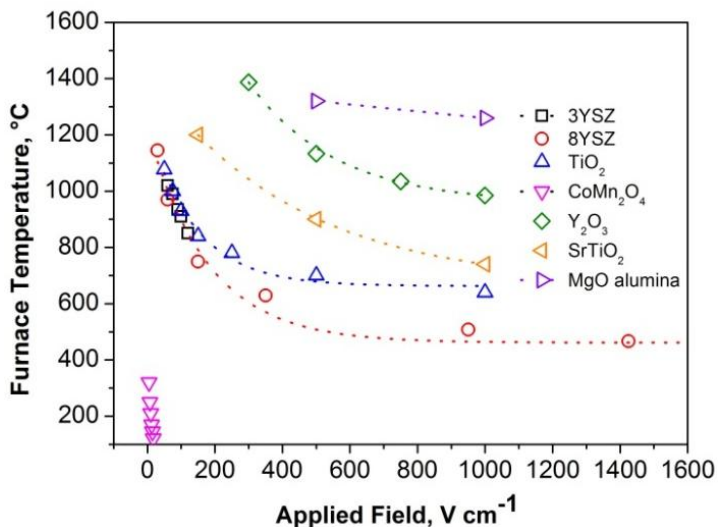
Fig. 7 Applied field verses furnace temperature for flash sintering of various oxides. [2,3,9,39,42–45]

Flash sintering can be carried out in two different sintering conditions. Either ramping the furnace at constant heating rate, where field is applied after binder burnout or by ramping the furnace at constant temperature and then applying constant applied field. In first case, threshold temperature activates the flash sintering while in later case flash sintering is accompanied by an incubation time. In both

16

conditions magnitude of applied electric field monitors the flash event. Most reported data for flash sintering are carried out by constant heating rate experiments.

The flash sintering is described by three major processes which occur simultaneously during flash event: Sudden shrinkage, rapid increase in power dissipation and photoluminescence.

Shrinkage and power dissipation:

The enlarge view of shrinkage strain and power during flash sintering of 3YSZ at 100 V cm^{-1} is shown in Fig. 8. The plot is divided into two parts; the upper portion of the plot represents shrinkage strain during the flash event, while the lower part describes power density (dissipation). Both this processes occurs at the same time scale. The power of the specimen rises to a maximum under constant voltage and then sharply decreases in current control mode where power remains in steady state. The sudden rise in conductivity of the specimen is an indelible signature of flash event. The current density can be controlled by switching the constant voltage of power supply to constant current mode. The line drawn at the centre of the power peak divides the sintering into two regimes. The experiment start at constant applied voltage to the specimen, which then increases non-linearly when reaches to threshold temperature. This is regime I, where power is given as V^2/R; as the resistance decreases the power dissipation of the specimen rises. Once power crosses the line, which is regime II where power is given as I^2R; the power now declines since the resistance continues to fall and approaches a steady state mode. The sudden shrinkage is also observed at the transition point and continues to shrink under current control mode.
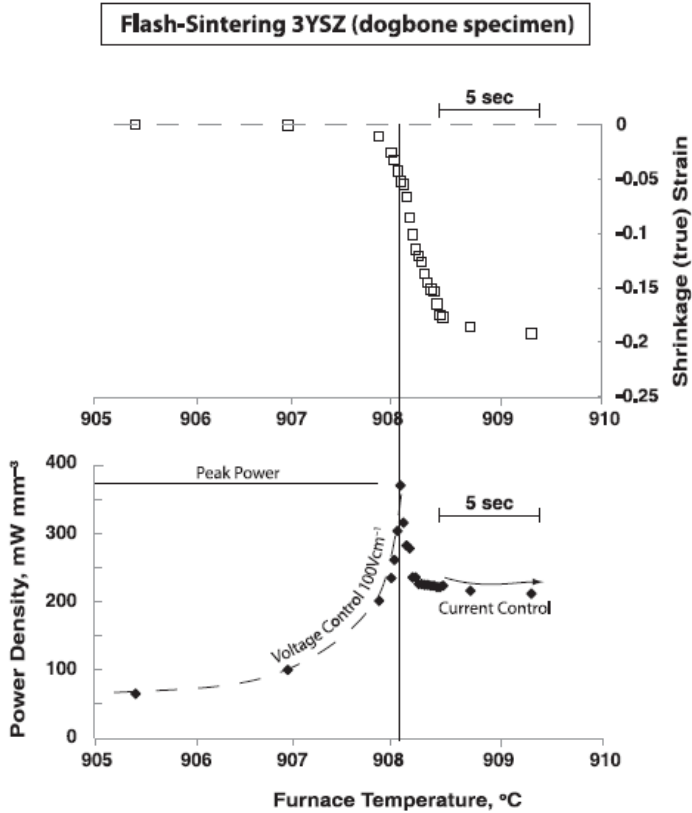
Fig. 8 Shrinkage and power dissipation during flash sintering of 3YSZ [46].

Photoluminescence:

The shrinkage and power is also accompanied by a growing specimen during the flash event. The process of flash sintering is also

seen in dense samples which much more intense glow in the speci-
men compared to porous sample. The initial report on photoemission
of dense samples is shown by Francis et al. [47]. The results of opti-
cal emission are shown in Fig. 9. The left plot shows optical emission
obtained for three different power inputs (shown at the right) in the
400 to 600 nm wavelength. The intensity increases with increased
power in the specimen. The reason behind this is not clear for the
present time, but could be related to joule heating.
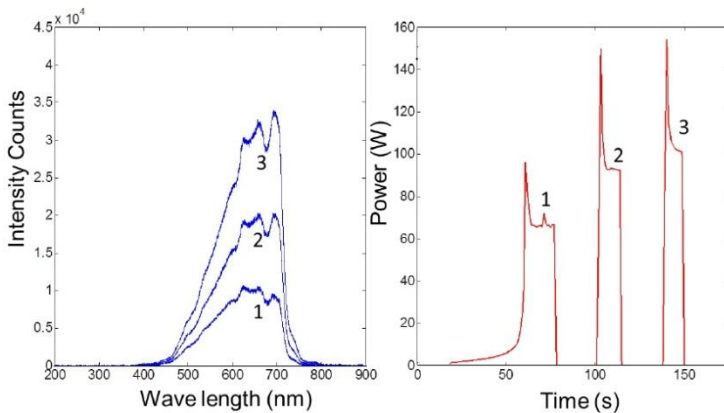
Fig. 9 Photoemission during flash sintering for three different power
surge values [47].

a) Joule Heating during flash sintering

Joule heating is defined as an increase in the specimen
temperature from the dissipation of electrical energy [48]. From the
experimental evidences, rise in power during flash event increases

the specimen temperature. An approximate way to estimate specimen temperature can be obtained by assuming specimen radiates like a black body. In the early demonstration of flash sintering, Cologna et at. estimated the specimen temperature based on black body radiation model as:

$$\frac{\Delta T}{T_0} = \frac{W}{4 A \sigma T_0^4} \qquad (3)$$

where ΔT is the increase in specimen temperature due to power dissipation W (in watts) of electrical energy, A is the surface area, σ is the black body radiation constant and T_0 is the furnace temperature.

From the results presented by Baraki et al. on 95 % dense sample of 8YSZ [49]. The increase in specimen temperature due to Joule heating can be also estimated from the volumetric thermal expansion. In their experiments, cylindrical specimen with 4 mm length with a diameter of 8 mm was subjected to known value power density at constant furnace temperature. The instantaneous expansion and contraction during on and off of the power density from 25 mW mm^{-3} to 400 mW mm^{-3} were observed and use to calculate the specimen temperature as:

$$\Delta T = \frac{1}{V_0} * \frac{\Delta V}{\alpha_{vol}} \quad (4)$$

where ΔT is the increase in specimen temperature due to Joule heating, V_0 is the initial sample volume, ΔV is the change in sample volume, and α_{vol} is volumetric thermal expansion coefficient of the sample.

The measurement from this analysis are in good agreement with the estimated temperature from the black body model as shown in Ref. [46] (Fig. 10).

20
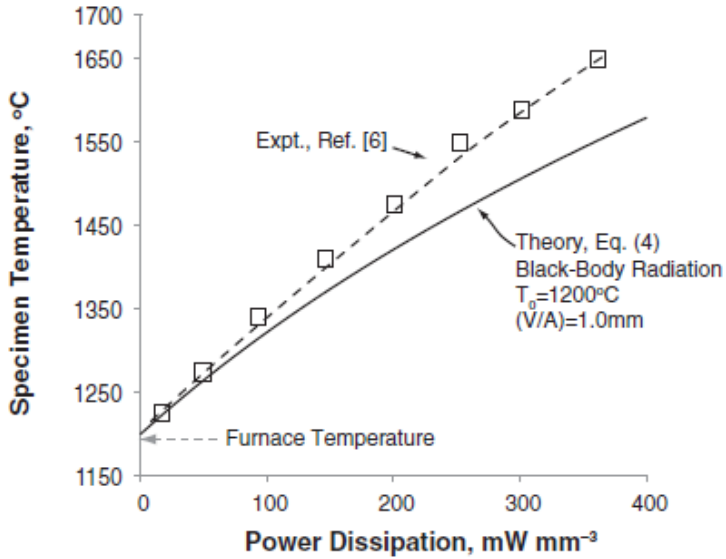
Fig.10. A comparison of specimen temperature from the experimental measurement of Baraki et. [49] and the black body radiation model estimated during Joule heating [46].

Another approach of measuring the specimen temperature is by focusing pyrometer on the surface of the sample. The pyrometer is first calibrated on the dense sample and then used for the measurement. The amount of power dissipated in the specimen determines the specimen temperature. The furnace temperature and pyrometer temperature remains the same until onset of power surge, and then it increases with power; and remains stable in the stable power regime. A temperature increase of ∼765°C is reported for 1445 mW mm^{-3} in case of MnCo2O4 (Fig. 11b), when the furnace temperature is at 210°C [40]. However, in case of 3YSZ at steady state power density of 125 mW mm^{-3}, temperature increases of ∼245°C (Fig. 11a) is observed at furnace temperature of 880°C [46].
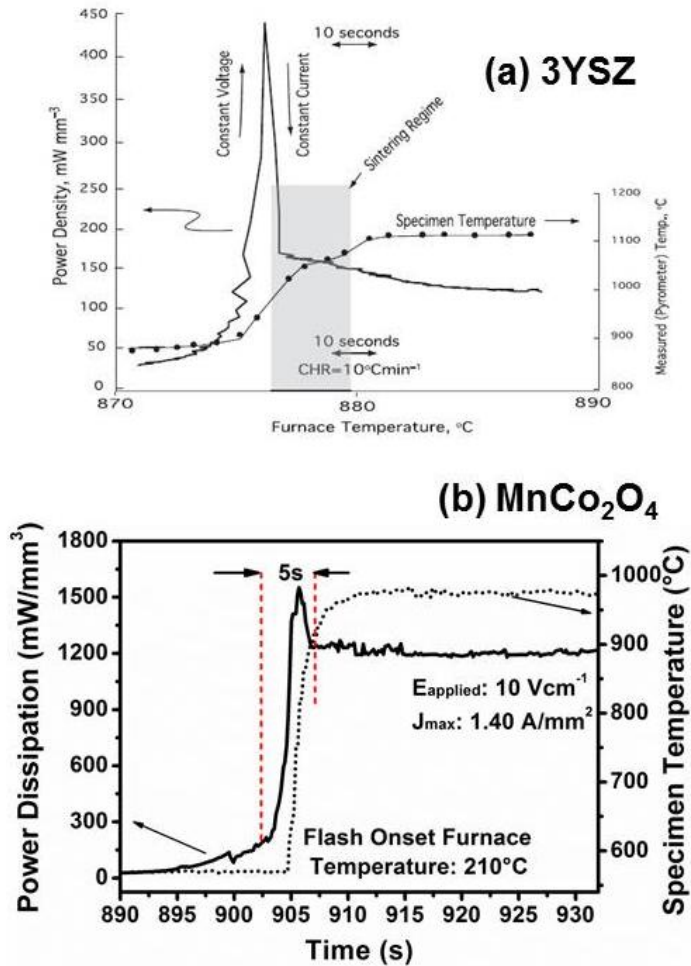
Fig. 11 Relationship between the power and the specimen temperature measured by pyrometer during (a) flash sinter-forging experiment in 3YSZ [46] and (b) flash sintering of $MnCo_2O_4$ [40].

b) Effect of field and current density on flash-sintering

The major driving force for flash sintering is the applied electric field. The flash effect can be induced by both DC as well as AC electric field. Most of the reported results above and also in this thesis are carried out by DC electric field. Here voltage and current density determines the final outcome of sintering. However, in case of AC electric field experiments magnitude of frequency along with voltage and current density controls the flash sintering process [7].

The current density plays a major role during flash sintering. The final density obtained depends on the current settings [5,7]. The experimental observation from Ref [5] is shown in Fig. 12. The experiments were carried out at constant furnace temperature (900°C) with an increased in current density from 20 to 100 mA mm^{-2}. At 20 mA mm^{-2} the final density reported to be $\sim$ 65 % which increases to full density at 100 mA mm^{-2} at constant applied voltage of 100 V cm^{-1}.
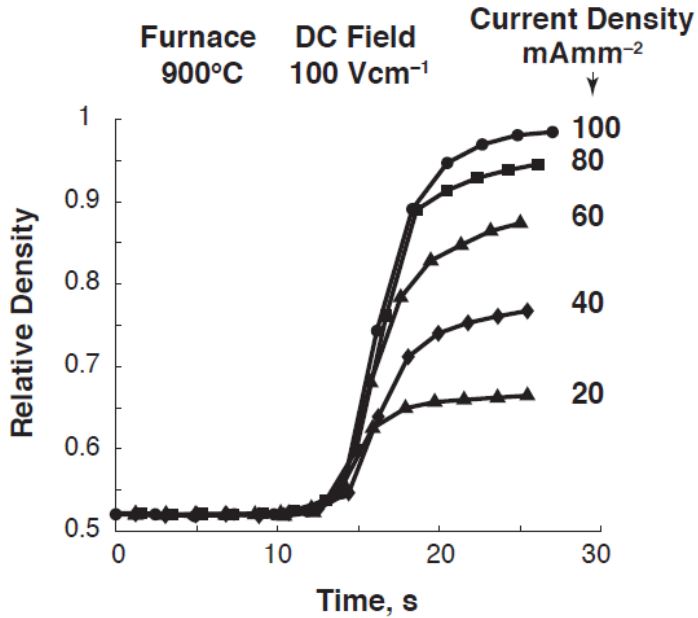
Fig. 12 Effect of current density during isothermal (900°C) flash sintering at 100 V cm^{-1}.

c) Effect of particle size on flash sintering

Initial particle size is also known to have influence on sintering kinetics. The particle must be homogeneously packed with a high packing density. The maximum number of particles contact increases the grain boundaries, thereby reduces the diffusion distance for rapid mass transport into the fine pores. This effect is also demonstrated by Francis et al. during flash sintering of 3 mol% Y_2O_3-stabilized ZrO_2 [50]. He used four different particle sized powders ranging from 1 µm to 10 µm and carried out flash sintering by applying 100 V cm^{-1}. Fig. 13 displays the shrinkage strain plot for 3YSZ flash and conventionally sintered for four different particle sizes. The observation pointed

out that, flash sintering temperature increases with the particle size. The most interesting finding from these results was the power dissipation and specimen temperatures (measured by pyrometer) were almost the same. Even though, the density decreases with increases in particle size.
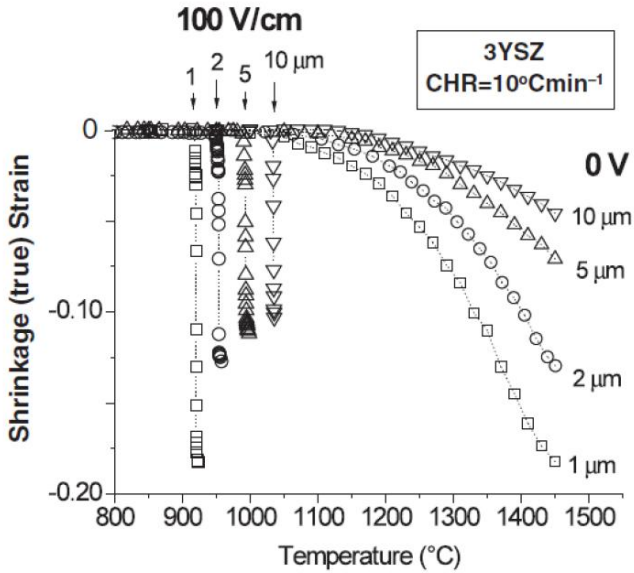
Fig.13 Shrinkage strain in the four particle size specimens at 0 V and 1000 V cm-1, measured as the furnace is ramped up at a constant heating rate of 10°C min-1 [50].

d) Influence of uniaxial applied stress on flash sintering

In case flash sintering, increased in applied electric field decreases onset temperature for sintering. Same is true with applied

pressure during sinter forging experiments. Typically, a uniaxial stress is applied to a powder or partially densified compact at the sintering temperature. Combined effect of flash sintering and sinter forging experiments where shown in Ref. [4], which is called as flash-sinter forging experiment. The pressure was applied along with the electric field as show in Fig. 14. The plate electrodes were used at the contact point between the load cells and the specimen.
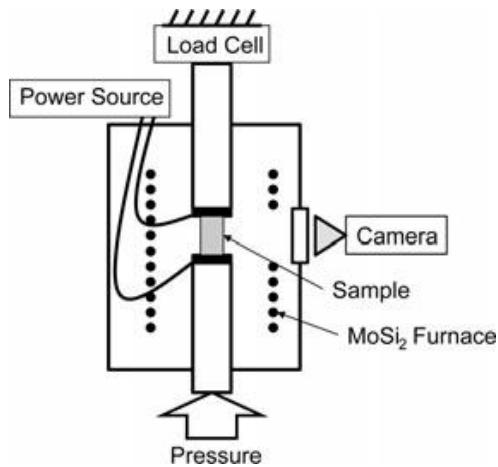
Fig. 14 Setup for flash sinter forging experiment [4].

Fig. 15 describes the densification strain during flash sinter-forging experiment of 3YSZ at 100 V cm^{-1} for different applied loads. For a constant applied electric field, Increasing the applied load (stressed) ranges from 1.5 MPa to 12 MPa decreases the sintering temperature. Flash sinter forging was also demonstrated at the constant applied load of 1.5 MPa, with varying applied electric field. Increasing the applied electric field reduces the onset of flash sintering, lower than normal flash sintering temperature.
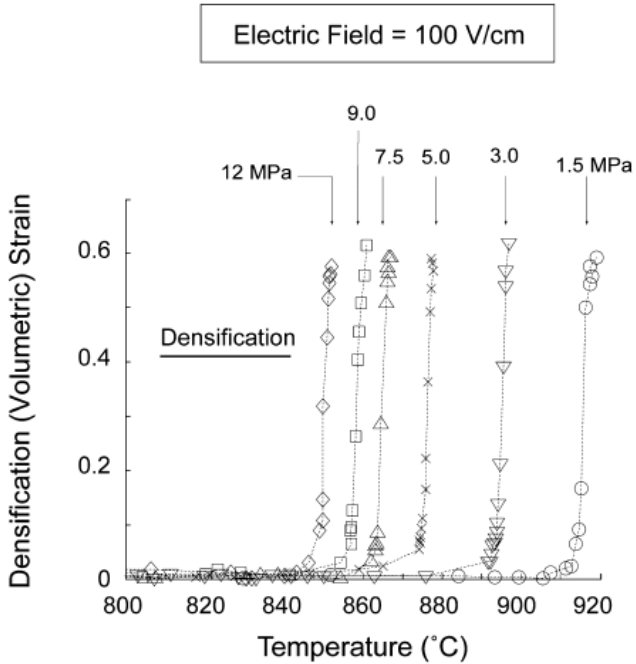
Fig. 15 Densification strain during flash sinter forging at 100 V cm^{-1} for different applied stresses [4].

e) Mechanism

Different mechanisms are proposed for electric field assisted sintering. The Joule heating was proposed as the cause for such an anomalous rapid sintering rate and high increase in specimen temperature. According to Narayana [51], the preferential ionic and electronic conduction along the grain boundaries results in Joule heating. This leads to enormous heating and selective melting of grain bound-

27

aries. This is proposed to be the primary mechanism involved for flash sintering.

However, according to the most common discussed mechanism based on the experimental evidences [6,9,48,50], Joule heating cannot be the only factor which can account for such a high sintering rate; specimen temperature required for sintering in seconds remains far lower than the estimated one [46].

Nucleation of Frenkel pairs was proposed to be the initial cause for flash sintering. The concept is that, vacancy-interstitial pairs of both anions and cations can ionize under electric field liberated hole and electron [45,50]. The vacancy and interstitial are now free to move within the lattice. So vacancy will migrate toward the grain boundary and interstitial towards the pore, resulting in charge transport and densification.

Chapter 3
Experimental Techniques

3.1 Starting Powders

3.1.1 α-alumina

High purity, ultra-fine and agglomerate free α-alumina powder (Taimicron TMDAR, Taimei Chemical Co., Ltd., Tokyo, Japan) was used throughout this study. The as received powder is specified to have primary particle size of 0.10 μm and a specific surface area (BET) of 14.5 m^2 g^{-1}. The powder can be nominally sintered to 3.96 g cm^{-3} at 1350°C. The purity of the powder according to supplier is given in table 2 [52].

Table 2. Purity and typical analysis of α-alumina.

Al_2O_3	Impurities (ppm)										
(%)	Si	Fe	Na	K	Cu	Mg	Cu	Cr	Mn	U	Th
> 99.99	10	8	8	3	3	2	1	<1	<1	< 0.004	< 0.005

3.1.2 Yttria stabilised zirconia (3YSZ)

Commercially available tetragonal zirconia (3 mol% yttria stabilized zirconia - 3YSZ) powder (TZ-3YS-E grade; Tosoh Corp., Shunan, Japan) was used for studies. The powder had particle size

of (D 50) 0.6 µm and granule size of (D 50) of 60 µm. The specific surface area (BET) and crystallite size were 7 ± 2 m^2 g^{-1} and 36 nm respectively. The sintered density of processed powder was 6.05 g cm^{-3}. The chemical characteristics of the powder is shown in table 3 [53].

Table 3. Chemical characteristics of 3YSZ

Chemical characteristics (wt %)	TZ-3YS-E
ZrO2 +HfO2+Y2O3+Al2O3	>99.9
Y2O3	5.15±0.20
Al2O3	0.25±0.10
SiO2	≤0.02
Fe2O3	≤0.01
Na2O	≤0.04
Loss on ignition (1000 °C)	≤1.2

3.1.3 Hydroxyapatite (HA)
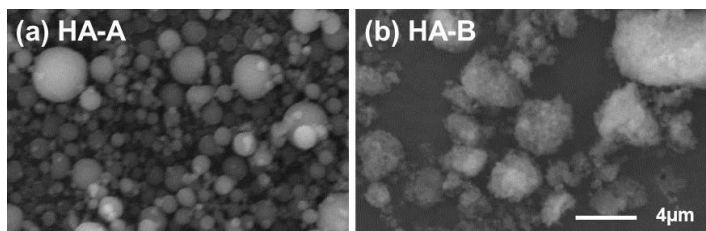
Fig.16. Hydroxyapatite (HA) powders used in this study (a) HA-A and (b) HA-B

Two commercially available hydroxyapatite (HA) powders were used in this study. The first, labelled as HA-A (nanoX-IM•HAp201, Fluidinova, Engenharia de Fluidos, S.A.), is spray-dried powder, with average particle size (D50) of 2.5 ± 0.5 µm. The HA was

extremely pure with very low concentration of heavy-metals (As <0.1, Hg <0.05, Cd <0.05, and Pb 0.5) [54]. The second one, named as HA-B (HA Lotto 80, Eurocoating, Italy), is agglomerated powder with particle size~2.0 µm. Figure 1 shows SEM images of both powders.

3.1.4 Magnesium nitrate and Ferric nitrate

MgO doped alumina and Fe_2O_3 doped alumina were prepared by using Magnesium nitrate hexahydrate (Mg $(NO3)_2.6H_2O$, Sigma-Aldrich) and Ferric nitrate (Fe (NO3)2.9H2O, Analyticals Carloerba) precursor respectively. The purity as per supplier is 99 % for both the precursor. The detailed doping procedure is discussed in the sub-section 4.5.

3.1.5 Binder

Commercially available Duramax B-1000 ceramics binder (Rohm and Haas France SAS, BP, France), ready to use as aqueous emulsion was used as binding agent in this study. The binder is supplied as pre-dispersed in water with 55% solids in it. It has low glass transition temperature (-26°C), density of 1.05 g/ml at 23°C, with pH in a range of 9.0-9.8 and viscosity of <140 cP (Brookfield # 2.60 rpm). The B-1000 binder has intrusting properties in enhancing strength of the green ceramic specimens. The weight loss profile of binder start at 350°C and end completely at 550-600°C [55]. The binder is added in weight percent according to solid content in the binder and not with respect to water based quantity.

The sample powder was mixed with required quantity of binder with sufficient distilled water for homogeneous mixing. The mixture was then dried overnight at 80°C and then ground to give fine powder.

3.2 Sample preparation

Figure 17a shows the high carbon stainless steel dog bone die used for pressing powders. The powder (either as received or doped or composite were mixed with 3 wt% binder (3.1.5)) was weighed and poured in the mold. The powder was then tapped for a period 10 s and uniaxially pressed in the die. The pressed sample was then ejected carefully and its dimensions were measured by Vernier calliper. A typical green dog bone pellet is shown in Fig 17b along with its dimensions.
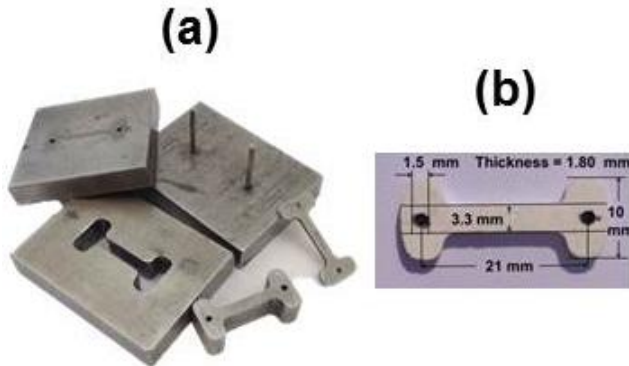
Fig. 17: (a) The Picture of the mold and (b) green dog-bone pellet after ejection.

3.2.1 Alumina zirconia composite

The 3YSZ/alumina composite samples containing 10, 20, 30, 40 and 50 vol% Al_2O_3 were prepared by mixing required amount of alumina (3.1.1) and 3YSZ (3.1.2) powders in distilled water. The suspension was dried and ground in a mortar. The powder was then mixed with 3 wt% binder (3.1.5) and deionized water. The mixture was dried in an oven at $80^{\circ}C$ and ground again to powder. Similarly,

3YSZ and α-alumina powders were mixed with 3 wt% binder (3.1.5), following the same procedure. The powders were then uniaxially pressed in dog-bone shaped pallets. For the samples used in section 4.1 and 4.2 have a relative green density of 52 ±1% for 3YSZ, 58 ±1% α-alumina, and 53±1% for the composite. The dimensions of the green sample are given is Fig. 2b. Whereas the samples used in section 4.3 have a relative green densities of the pressed samples, given at increasing concentration of Al_2O_3 were 48 ±1%, 48 ±1%, 48 ±1%, 49 ±1% and 50 ±1% respectively.

3.2.2 Hydroxyapatite

Two commercially available HA powders discussed above (3.1.3) were mixed with 3 wt% binder (3.1.5), with sufficient amount of deionised water. The resulting slurries were dried overnight at 110°C in an oven. The cakes were then ground to powder which were uniaxially pressed in to dog-bone shaped samples at a pressure of 120 MPa. The relative density of the green samples was 44±1% ($\rho_{theoretical}$ = 3.16 g cm^{-3}). The samples obtained were 21 mm long with rectangular cross section of 3 mm width and 1.78 ±0.03 mm thickness.

3.2.3 Undoped and doped alumina

The starting material used was un-doped alumina (3.1.1). MgO and Fe_2O_3 doped alumina were prepared with two different concentrations: 0.5 wt.% and 1.0 wt.%. The doping was performed by adding the alumina powder to a solution of Magnesium nitrate or ferric nitrate (3.1.4) and deionised water [56,57]. The proportioned powder mixture was wet milled for 12 h in deionised water using a polyethylene bottle and high purity alumina balls. The suspensions were oven dried, ground to powder and calcined at 800°C for 2 h in order

to decompose nitrate. The un-doped alumina (3.1.1) and doped alumina powders were then mixed with 3 wt.% binder (2.1.5) and pressed in to a dog bone pellet (Fig. 4) in order to use for flash sintering experiments.

3.3 Experimental set up for flash sintering

The experimental arrangement for flash sintering is sketched in Fig. 18. The flash sintering or two electrode sintering behavior is measured by suspending the dog bone sample into the furnace. The platinum wire serves as electrode and also acts as current carrier in the circuit. The setup is made up of different components.
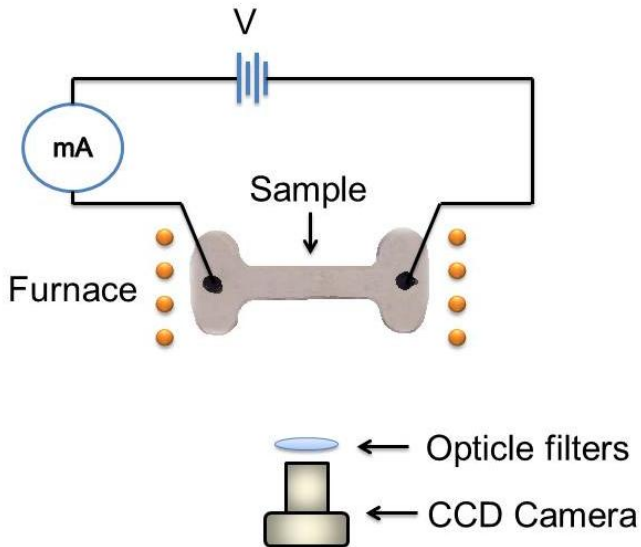
Fig.18. Flash sintering setup and dimensions of dog bone pellet.

3.3.1 Furnace

Two types of tube furnaces were used in this study. One was vertical and other was horizontal tube furnace. All the furnaces

used are electrical resistance furnaces, in which current carrying resistor, called the furnace element or winding, serves as the source of heat. Fig. 19 provides the different furnaces used and its experimental setup. The furnace shown in Fig. 19a was manufactured by Deltech Inc. (Denver, CO) with 50 mm diameter alumina tube [47]. The furnace elements were made up of $MoSi_2$ and temperature was controlled by Eurotherm 2404 PID temperature controller, with B-type thermocouple. Whereas, the furnaces shown in Fig. 19b (RT 50, R&D Srl, Mazzo di Rho, Italy) and Fig. 19c (HTRH 100-300/18, GERO Hochtemperaturöfen GmbH, Germany) are manufactured by Nabertherm, with a tube diameter of 40 mm and 100 mm respectively, and the temperature was controlled by in build programming software provided by the manufacturer. The sample temperature is also measured by s-type thermocouple which was places 0.5-1 cm away, in order to protect it from joule heating, which was observed during flash sintering. The specimen is suspended in the tubular furnace exactly at the center of the heating zone.
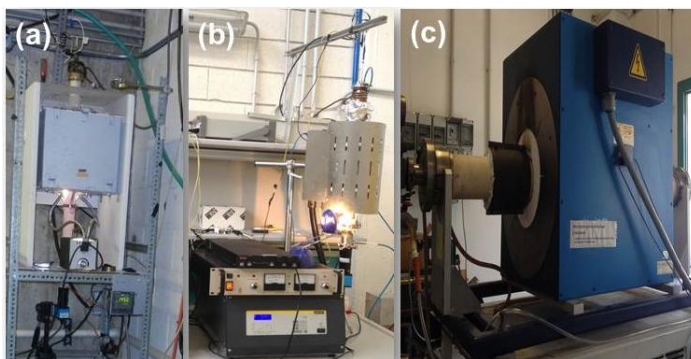
Fig.19. Furnaces used for the flash sintering experiments.

35

3.3.2 Digital Multi-meter

The current flowing through the circuit was monitor by Keithley 2000 or Keithley 2100 and was connected to the programing software by means of GPIB interphase (Keithley 2000) or USB (Keithley 2100).

3.3.3 Power supply

The electric field required for flash sintering was supplied by power supply. Different power supplies were used due to the limited voltage applicable by some power supplies. The Sorensen DLM300-2 has a power limit of maximum 300 V and maximum current capacity of 2 Ampere. The other power supplies used were Glassman EW05R120 high voltage power supply (Max. 5 KV and 120 mA) and Glassman FJ2P60 (Max. 2 KV and 60 mA). Sampling of applied voltage data was done with the help of NI USB 6009 interphase.

3.3.4 CCD camera

The sintering was monitor by CCD camera (Imaging Source DMK 41-AU02), focusing on the sample through optical filter (Edmund Optics Ltd) and fused silica window (Edmund Optics Ltd). The images were captured in the form of Avi file and then deframe it into images at regular intervals. The camera can also collect images at 0.5 to 1 frame per seconds. However in video mode, it can go up to 16 frames per second [47].

3.4 Experimental procedure

3.4.1 Flash sintering of 50 vol% 3YSZ/Al$_2$O$_3$ composite

a) Constant heating rate (CHR)

The experimental setup (Fig. 18) for flash sintering is described above (Fig. 19a) used for the flash sintering experiments. The specimen is suspended in the hot zone of a tubular furnace by two platinum electrodes, which also serve to carry electric power to the specimen. The platinum wires were connected at the handles of the specimen with platinum paste to make good electrical contact and facilitate a uniform current flow through the gage-section of the dog bone specimen. Note that the platinum paste was used only at the electrode contact that is at the two holes of the dog bone, and not on the entire gage-section of the dog bone sample.

The sintering experiments were carried out by pre-heating the specimens at 600°C for 1 h to remove the binder. After binder burnout, the electric field was applied and the furnace was ramped with heating rate of 10°C min^{-1} up to 1400°C. The influence of fields up to 150 V cm^{-1} was investigated.

The onset of flash sintering is accompanied by a sudden increase in conductivity. This increase in conductivity was interrupted by switching the power supply from voltage control to current control.[46] The constant current condition was maintained for 60 s, after which the power supply was turned off and the furnace was cooled down to room temperature at 25°C min^{-1}.

Conventional sintering experiments (without electric field) were carried out in a box furnace. These specimens were sintered at five different temperatures (1600°C, 1650°C, 1675°C, 1700°C,

1750°C) using the same ramping rate as that of flash sintering exper-
iments followed by holding at the maximum temperature for 60 min.

b) Isothermal flash sintering

The same experimental setup was used (Fig. 19a) for iso-
thermal flash sintering of 50 vol% 3YSZ/Al$_2$O$_3$ composite. The similar
initial procedure was followed up to binder burnout. Thereafter, the
furnace was heated at a rate of 10°C min^{-1} up to the required temper-
ature, and then held at this temperature for isothermal experiments.
Experiments were performed at four temperatures, 1000°C, 1200°C,
1275°C and 1300°C. The DC electric field was applied after holding
the specimen at temperature for 30 minutes. The onset of the flash
(after an incubation time) was accompanied by a non-linear increase
in conductivity, which was controlled by switching the power supply
from voltage to current control [46]. Thereafter, the constant current
condition was maintained for 60 s, before the power supply was
switched off.

3.4.2 Effect of alumina addition on flash
sintering of alumina-zirconia composite

The experimental setup for flash sintering (Fig. 18) was
done in vertical tubular furnace (fig. 19b). Similar experimental proce-
dures were followed as shown in section 3.4.1.1 for CHR experiments
and 3.4.1.2 for isothermal flash sintering experiments of composite.
The two holes of the dog bone sample were connected to the hock of
the platinum electrode and placed into the hot zone of the furnace.
The furnace was first ramped at 5°C min^{-1} up to 600°C and main-
tained for 1 h in order to completely burnout the binder. After that the
furnace was programed accordingly.

For constant heating rate experiments (CHR), a constant field of 150 V cm^{-1} was applied after the binder burnout while ramping the furnace at 10°C min^{-1} until specimen shows flash sintering. The flash onset was controlled by switching the power supply from voltage to current control. Once flash sintering was done, furnace was turned off and allowed to cool.

In case of isothermal flash sintering experiments, after the binder burnout step, furnace was ramped to up to 1100°C (10°C min^{-1}) and E-field of 150 V cm^{-1} was applied after 15 min of stabilisation. The time at which field was applied was considered as zero time. After a certain incubation period the flash sintering was observed. Once flash sintering was done, furnace was turned off and allowed to cool.

3.4.3 Flash sintering of Hydroxyapatite

The set up and procedure for flash sintering similar to those described in section 3.3 [9,58] was done in a horizontal tubular furnace (3.3.1) by hanging the dog-bone sample vertically in the hot zone (Fig. 4c). The sample was hung by two platinum electrodes (0.5mm diameter) which served to hold the sample in hot zone and also to the apply electric field. Dry, artificial air was fluxed through the furnace during the measurements in order to maintain dry atmosphere to prevent electrical arching between electrodes at high voltages. The furnace temperature was measured by s-type thermocouple held in the hot zone, but far enough from the sample to not be influenced by the joule heating that is known to occur using this method [46]. The desired E-field was applied with Glassman EW05R120 high voltage power supply. Once the current density rises nonlinearly the power supply was switched off and sample was allowed to cool down normally to room temperature. The current passing through the sample was monitored by a Keithley 2000 DMM.

Experiments were carried out by ramping the furnace at 10°C min^{-1} until 1400°C at a particular electric field. The electric field applied was between 0 V to 2000 V cm^{-1} in steps of 500V cm^{-1}.

3.4.4 Flash sintering of undoped and doped alumina

The experimental procedure remains the same as describe for constant heating rate experiment before. In case un-doped alumina the electric field of 1500 V cm^{-1} and 1750 V cm^{-1} were used for flash sintering, whereas for doped alumina flash sintering was analysed at 1000 V cm^{-1}.

3.5 Characterization

3.5.1 Shrinkage and Density

The shrinkage in the specimen was measured from photographs taken with a CCD camera at a rate of once every minute before, and at 1 s intervals after the onset of the flash. The shrinkage was calculated in the form of linear strain. The linear strain or true strain is defined as $\varepsilon = \ln\left(\dfrac{\ell}{\ell_0}\right)$, where ℓ_0 is the initial length and ℓ is the length after time t (or temperature T). To determine the sintering kinetics, the true strain at several times or temperatures is measured, giving a plot of true strain versus sintering time or temperature. The length ℓ was calculated from the photographs acquired from CCD camera at regular time intervals.

The density of the green samples was determined from mass and dimensions (volume) of the sample. However the final den-

sity of the sintered samples was calculated by Archimedes method using water as fluid. During flash sintering only the rectangular bar of the dog bone undergoes sintering, whereas the ears of the dog bone remains un-sintered. The rectangular bar of the dog bone were cut using diamond blade and used for analysis. The standard test method as described in ASTM C 830-00 was used to determine the bulk density (B) of the test specimen as the ratio of its dry weight to exterior volume.

$$B = \frac{D}{V} \qquad (4)$$

where D is its dry weight and V is its exterior volume

All the weights were measured by scientific weighing balance (Gibertini Analytic Balance). In order to calculate the exterior volume, the specimen was first vacuum socked in de ionised water for 2 h. The sample was then suspended in water and its weight was measured. The balance was equipped with a setup to measure suspended weight. After obtaining the suspended weight of the sample, the surface water was carefully removed with moistened smooth linen and sample was weighted in order to get saturated weight. Now the exterior volume was calculated by subtracting the suspended weight from the saturated weight. After all the measurements the sample was dried overnight at 110°C and compared to the initial dry weight.

3.5.2 Scanning electron microscopy

The starting powders and final microstructures were examined using a JEOL JSM-5500E Scanning electron microscopy (SEM). The samples were first coated with a layer of gold–palladium by sputter coating for 90 seconds. For powder and fractures sample images were observed using accelerating voltage of 10 kV, while for grain size measurement images were observed at 5 kV accelerating volt-

age.

3.5.2.1 Grain size

The average grain size and the standard deviation was determined directly from the SEM micrographs with lineal-intercept analysis [59,60].

a) Sample preparation

The samples obtained after consolidation were cross sectioned exactly at the middle of the dog bone and then mounted into acrylic resin. The cross section was then polished at different abrasive tapes in order to obtain mirror fine polished cross section. The detailed procedure for sample sawing, mounting on resin and polishing is discussed in ref. [61]. The samples obtained after polishing were used for thermal etching at 1350°C. The temperature for thermal etching was selected by first etching conventionally sintered sample (1600°C for 1 h) at different annealing temperature for 30 min. The specimens prepared at 0 V to 40 V cm^{-1}, which did not sinter significantly, were thermally etched at a lower temperature (1200°C) to prevent grain growth.

b) Grain size measurement

The common procedure in calculating grain size by lineal intercept was used. The method involved measurements on microstructural images of thermally etched polished sample with clear visibility of its grain boundaries. The test line was drawn on the micrograph with known distance and number of grains (intercept) or grain boundaries (intersections) intersecting the line was counted. The average grain size for single phase sample is given as:

$$D = 1.56 \frac{C}{MN} \qquad (5)$$

Where D is the average grain size, C the total length of test line used, M is the magnification of the micrograph and N the number of intercept on the test line. The constant 1.56 is derived by Mendelson [59] for random slices of tetrakaidecahedrally shaped grains.

The above formula was then modified by Wurst and Nelson [60] for two phase system. In order to calculate the actual grain size on randomly distributed second phase, correction is to be needed in both the test line intersection on interphases and the number of grains on the intercept. The modified length of the test line and the effective number of intersecting boundaries are calculated according to the new formulas for two phase system:

$$C_{eff} = C(1 - \nu) \qquad (6)$$

$$N_{eff} = N_{aa} + \frac{1}{2} N_{ab} \qquad (7)$$

Where C_{eff} is the modified length of the test line, C is length of the drawn line, ν is the volume fraction of the second phase, N_{eff} is the effective number of intersecting boundaries, N_{aa} is the number of in-tercepts with the boundaries with continuous grain of primary phases, and N_{ab} is the intercepts with the boundaries between primary phase and secondary phases.

Now the modified lineal intercept for grain size analysis of two phase system is given as

$$G = 1.56 \frac{C_{eff}}{MN_{eff}} \qquad (8)$$

The grain size analysis was carried on 5-6 micrograph of the same sample at different places of the cross section. Each micro-graph was analysed by counting at least 10 minimum test lines.

The grain size was also analysed using MATLB (GUIline-cut). The program allows us to analyse the size of grains in a micrograph with the line cut method arrangement. After loading the micrograph the program draws the lines on the surface. The number of grain boundaries intersecting the line were counted by clicking the cursor on the intercept.

3.5.3 XRD analysis

The phase analysis was carried on powder as well as sintered pellets by using X-ray diffractometer (Rigaku DMax - Bragg-Brentano configuration). Powder sample was ground to a fine powder and placed on the sample holder. For flash sintered samples the ends of the sintered dog bone were cut using a diamond saw and the sintered rectangular part was used for analysis. The specimens were exposed to CuK-α radiation source with step size of 0.02° with the hold time of 6 s at each step.

3.5.4 FTIR spectroscopy

Infrared (IR) spectra were measured using a Fourier transform Infrared spectrometer (Nicolet Avatar 330, Thermo Electro Corporation, Waltham, MA). The sample were mixed solid KBr, then ground and pressed to pellet. An average of 64 scans with 4 cm^{-1} resolution was recorded for each sample.

Chapter 4
Results and Discussion

4.1 Flash sintering of 50 vol% 3YSZ/Al$_2$O$_3$ composite (CHR)

4.1.1 Results

a) Conventional Sintering

Fig. 20. Conventional sintering of 3YSZ, alumina and 3YSZ-alumina composite.

Data for conventional sintering (0 V) are plotted in Fig. 20. In these experiments the samples were heated up to 1400°C at a constant heating rate of 10°C min^{-1}, without any isothermal hold time upon reaching this temperature. The linear shrinkage strains are plotted as a function of temperature. Alumina begins to sinter at ~1100°C, while in 3YSZ sintering starts at ~1150°C although they follow a dif-

ferent sintering behavior as the temperature rises. The 3YSZ-alumina composite begins to sinter at a higher temperature, about 1200°C. The sintering rate of the composite is much lower than either of the single-phase materials.

b) Field Assisted Sintering

Electric field assisted sintering results for the pure phases are shown in Fig. 21a, on the left. Pure alumina shows no effect at fields of up to 150 V cm^{-1}. In contrast the flash behavior of 3YSZ is exemplified by the vertical slopes of the shrinkage profiles. Flash sintering is seen at ~970°C at a field of 50 Vcm^{-1}. A higher field lowers the flash temperatures. At 150 V cm^{-1}, 3YSZ flash sinters at a furnace temperature of ~750°C.

The influence of electric fields on sintering of the composites is shown in Fig. 21b. Initially they show FAST behavior, where the density increases gradually with temperature, which is followed by flash sintering. This dual behavior is being called "hybrid sintering". It is seen in the range of 50-100 V cm^{-1}. At 150 V cm^{-1} sintering occurs predominantly in the flash mode.

In conventional sintering (0 V) the composite specimen shows a shrinkage of only 6% at 1400°C. The sintering is somewhat enhanced at applied fields of 30 V cm^{-1} and 40 V cm^{-1}, yielding shrinkage strains of 6.7% and 8.2%, respectively. When the applied field is increased to 50 V cm^{-1} the shrinkage rate increases further and sintering is completed at about ~1380°C, with a final shrinkage of 18.8%. Further increase of the electric field to 75 V cm^{-1} and 100 V cm^{-1} produces a rapid increase in the shrinkage rate. At 150 V cm^{-1}, the composite sinters abruptly to near full density at ~1060°C. The final density of all the flash sintered samples was higher than 95 %, while in case of 0 V - 40 V cm^{-1} the final density was less than 80%.
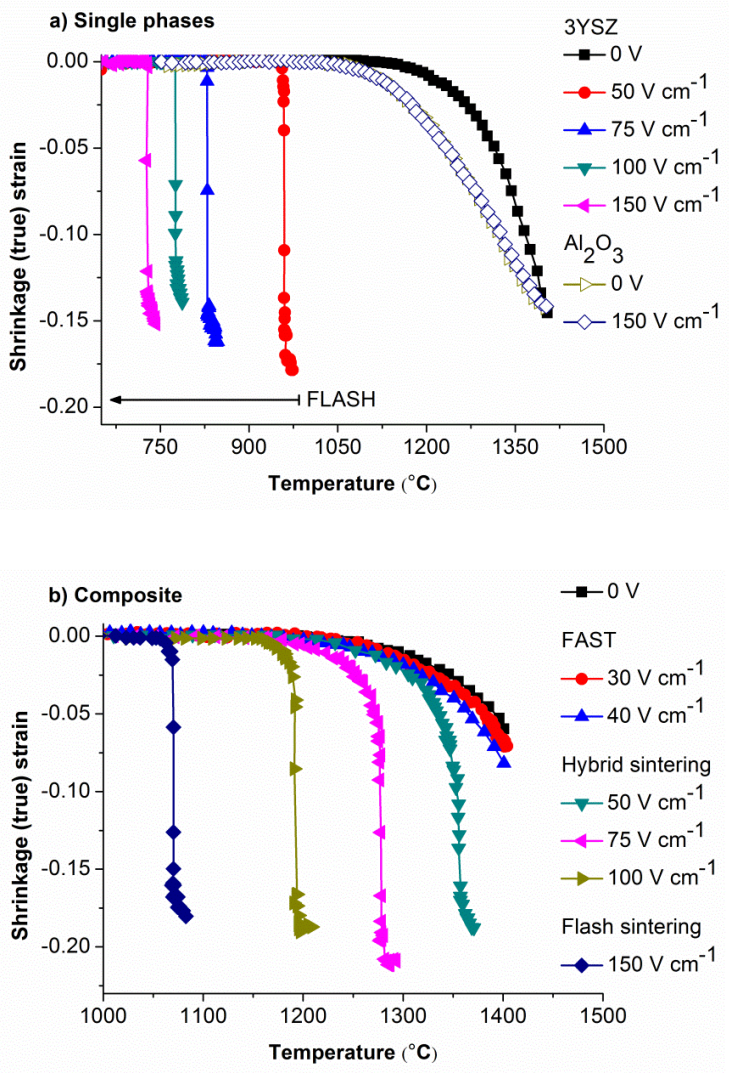
Fig. 21 Shrinkage plot of a) single phases of 3YSZ and alumina (top) b) 3YSZ/alumina composite (bottom) as a function of furnace temperature.

48

c) Joule Heating

In ceramic oxides, the increase in conductivity generally follows Arrhenius behavior. The onset of flash, however, is accompanied by an abrupt increase in the conductivity, as shown in Fig. 22. The power supply is then switched to current control to limit the Joule heating of the specimen. In present experiments current density was set 85 mA mm^{-2}. The power dissipation in the specimen, *P,* is calculated from $P = E\,j$ where E is applied electric field (V cm^{-1}) and *j is* the current density (mA mm^{-2}).

At low fields of 30 V cm^{-1} and 40 V cm^{-1} the composite does not show significant field assisted sintering (Fig. 22b). At 50 V cm^{-1}, the power increases Arrheniusly up to ~1340°C and then abruptly, which is characteristic of a flash event. Similar behavior is seen at 75 V cm^{-1}, but the onset of the non-linearity is shifted to a lower temperature. At 100 V cm^{-1} and 150 V cm^{-1} the non-linearity occurs at ~1185°C and 1040°C. However, the current may increase only up to the current limit set at the power supply. Under current control the power dissipation declines and approaches a steady state.

Typical behavior of the power dissipation and the true strain as a function of time for the case of 100 V cm^{-1} is shown in Fig. 23a, for single-phase 3YSZ, and in Fig. 23b for the composite. Power dissipation, calculated from experimental values of the voltage and the current are shown. The peak value measured at the transition from voltage to current control is equal to 400 mW mm^{-3}. Once the power supply is switched to constant current, the power dissipation declines to ~160 mW mm^{-3} for 3YSZ and ~243 mW mm^{-3} for the composite. The onset of shrinkage is synchronous with the sudden increase in the power dissipation.
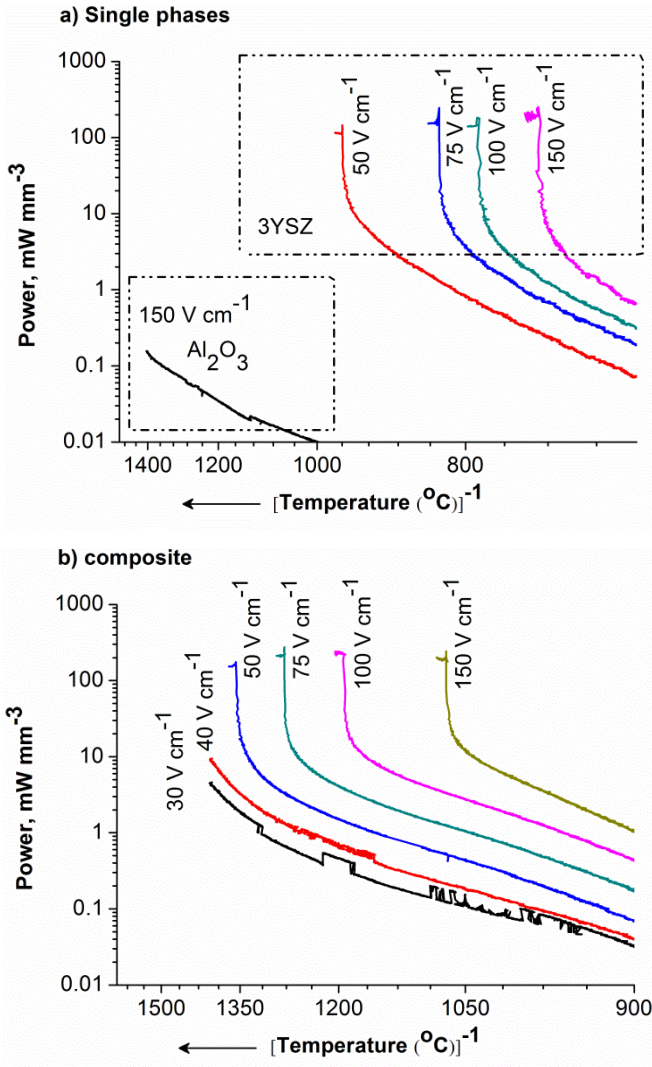
Fig. 22. Arrhenius plot for the power dissipated in a) single phases (alumina and 3YSZ) and b) 3YSZ-alumina composite as a function of furnace temperature under different applied voltages.
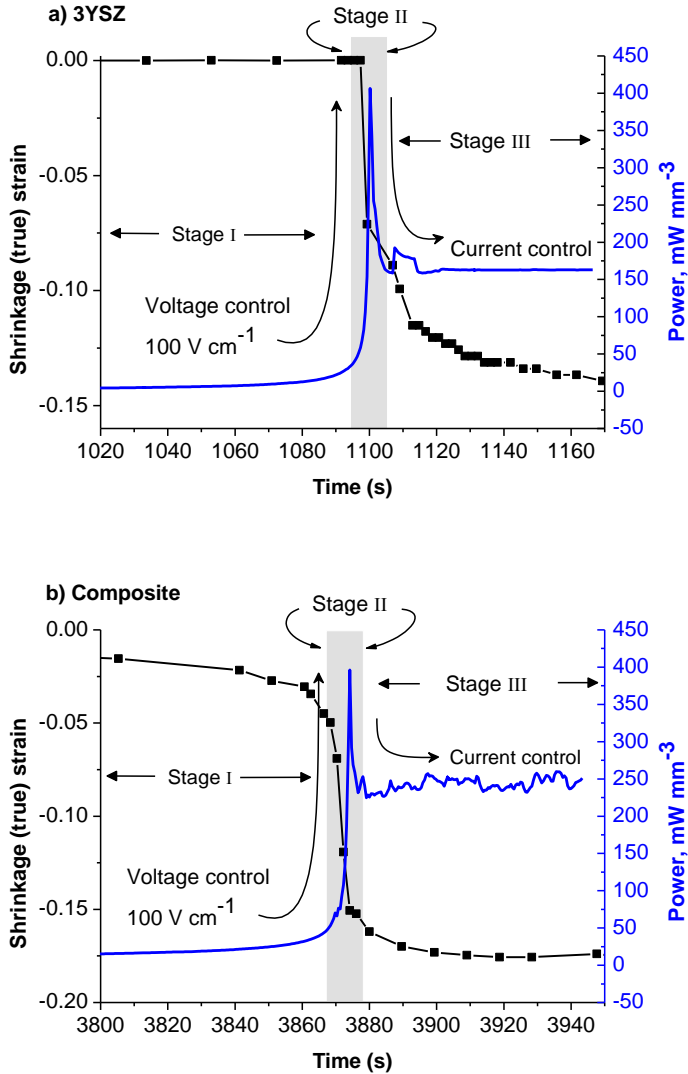
Fig. 23. Power density and shrinkage strain as function of time for flash sintering of a) 3YSZ (left) and b) 3YSZ/alumina composite (right) under 100 V cm^{-1}.

The shape of the power dissipation curve may be divided into three stages, the pre-flash stage, called Stage I, the transient stage which includes the peak in the power dissipation and the onset of the flash, Stage II, and the quasi-steady state regime under current control, which is Stage III. In Stage III the samples remain in a state of flash. They are then close to full density, yet, as shown later, grain growth occurs at a much faster rate than in conventional sintering.

Table 4. Power values for flash sintering of 50 vol% 3YSZ-alumina composite at different applied E-field.

Electric field (Vcm^{-1}) Stage I	Max power (mWmm^{-3}) Stage II	Steady state power (mWmm^{-3}) Stage III	Furnace Temp. for on-set of flash (°C)	Flash Temp. (°C)	Hold time during steady state (s)
50	200	156	1337	1360	60
75	300	212	1256	1280	60
100	400	243	1170	1205	60
150	600	192	1040	1060	60

The maximum power dissipation in Stage II and the power dissipation in Stage III are summarized in Table 4. The table includes data for the applied electric field and furnace temperature at the onset of the flash. The maximum power increases as the field increases, as it must since it is equal to the product of the applied field and the current limit, which was held constant for these experiments. The data in

Stage III shows scatter without a consistent trend. A correlation of these data with Fig. 21 suggests that the samples continue to sinter in Stage III if the steady state power is below 200 mW mm^{-3}, but there is little further shrinkage when the power dissipation is more than 200 mW mm^{-3}. This is partly because at higher current densities the sample sinters more completely during the transient (Stage II).

Joule heating is an important effect that accompanies the flash event. The specimen temperature rises with the dissipation. The detailed analysis of Joule heating has been reported in ref.[46], where an approximate increase in specimen temperature is calculated from a black body radiation model given by

$$\frac{T}{T_F} = \left[1 + \frac{1000W_V}{\varepsilon\sigma T_F^4}\left(\frac{V}{A}\right)\right]^{\frac{1}{4}} \qquad (9)$$

where T is the actual temperature of the specimen, and T_F is the furnace temperature in Kelvin. The steady state power dissipation per unit volume of the specimen is given by W_V, in units of mWmm^{-3}. The volume to surface area of the specimen is (V/A) written in units of mm (for our samples it value is equal to 0.5 mm). σ is black body radiation constant, being equal to 5.67 × 10^{-8} W·m^{-2} K^{-4}. The emissivity of the materials is given by e. We assume it to lie in the range 0.73 – 0.92 drawing upon the literature on thermal barrier coatings made from YSZ [62]. The range of specimen temperatures estimated in this way is reported in Table 6.

d) Microstructure

The flash sintered specimens were polished and thermally etched at 1350°C for 30 min and observed under SEM. The micro-structures of 3YSZ-alumina composites sintered under different applied fields are shown in Fig. 24. The dark phase corresponds to alumina and the brighter phase is zirconia. Conventionally sintered specimen and the specimen sintered at low fields (0 V to 40 V cm^{-1}) at temperatures up to 1400°C show similar microstructure with few pores and an average grain size of ~100 nm; note that these samples were only 80% dense. At fields greater than 50 V cm^{-1} the samples show a nearly fully dense microstructure. The microstructure is an intimate mixture of two distinct interpenetrating phases that are uniformly dispersed.

The grain size values are summarized in Table 5 and 6. The values for conventional sintering were measured after an isothermal hold of 60 min at the temperatures shown in the table. Those for flash sintering were obtained from samples held in Stage III for 60 s. In conventional sintering the grain size continues to increase with temperature. But in flash sintering the grain size becomes smaller as the field rises. Note that the grain size of conventionally sintered sample, at 1750°C, is close to the value obtained at a much low temperature under a field of 50 V cm^{-1}.
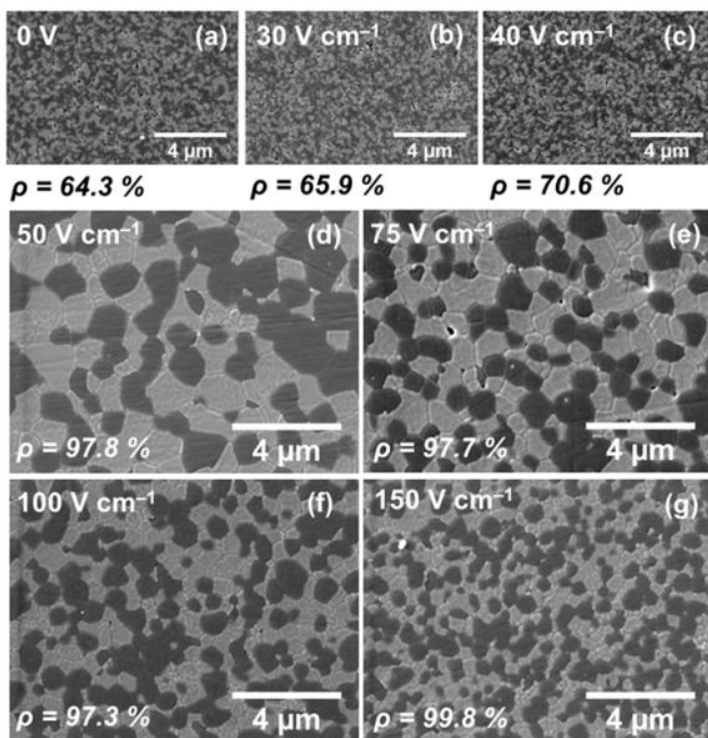
Fig. 24. Microstructure of 3YSZ-alumina composite at different applied voltages a) 0 V b) 30 V cm^{-1} c) 40 V cm^{-1} d) 50 V cm^{-1}, e) 75 V cm^{-1}, f) 100 V cm^{-1} and g) 150 V cm^{-1}. ρ = final density of sintered samples.

Table 5. Grain size data for individual phases of composite for conventional sintering.

Conventional sintering		
Grain size (nm)		Furnace temperature (°C)
Al_2O_3 G_{11}	ZrO_2 G_{12}	
829 ± 40	757 ± 67	1600
1039 ± 96	906 ± 73	1650
1087 ± 43	964 ± 125	1675
1415 ± 122	1248 ± 89	1700
1652 ± 91	1610 ± 232	1750

Table 6. Grain size data for individual phases of composite with specimen temperature measured by black body model for flash sintering.

Flash sintering				
E-Field ($V\ cm^{-1}$)	Grain size (nm)		Specimen temperature (°C)	
	Al_2O_3 G_{21}	Al_2O_3 G_{21}	$\mathcal{e}$ = 0.92	$\mathcal{e}$ = 0.73
50	1455 ± 238	1302 ± 298	1449	1470
75	1209 ± 231	939 ± 163	1414	1444
100	950 ± 77	813 ± 72	1375	1412
150	772 ± 135	652 ± 122	1238	1276

e) Analysis of Grain Growth

The influence of electric fields on grain growth falls into two regimes. At weak fields, that are below the threshold for flash, it has been conclusively shown that grain growth is retarded [63]. Indeed the increased rate of sintering in the FAST regime has been explained in terms of the reduced rate of grain growth [64].

However, in the flash regime, where the electric fields are large, grain growth is significantly enhanced, as shown here. We have studied this regime by examining grain growth in Stage III where the specimens remain in the flash state and at an isothermal temperature since the power dissipation in the specimen remains reasonably constant as shown in Fig. 25.
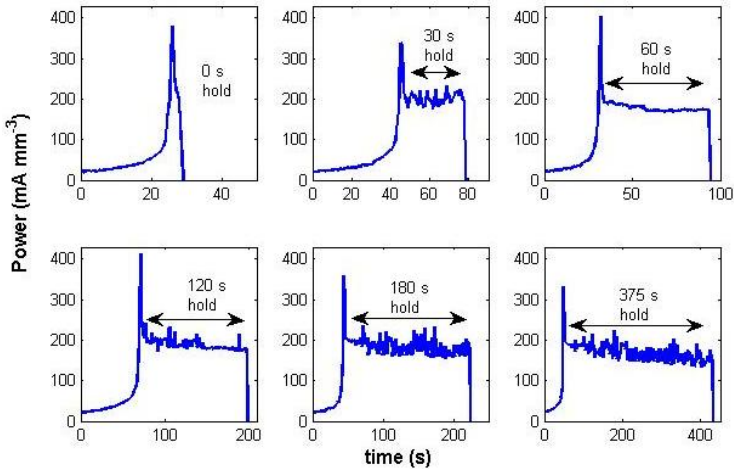
Fig. 25 Power plot of flash sintering at different post flash sintering time under 100 V cm-1 at current density of 84 mAmm-3

Both sets of data are analyzed in the conventional way by the following, well established procedure [65,66] where grain growth is described by

$$G_{ij} = A_{ij} t^{n_{ij}} \exp(-\frac{\Delta H_{ij}}{RT}) \qquad (10)$$

where G is the grain size, t is the time at constant temperature, ΔH is the activation energy, and A is the pre-exponential material parameter. The subscripts ij are used to distinguish between differ-ent cases. Thus, $i = 1,2$ refers to conventional ($i = 1$) and flash ($i = 2$) respectively. And, $j = 1,2$ refers to alumina grain size ($j = 1$) and the zirconia grain size ($j = 2$). For example n_{21} refers to the grain size exponent for alumina grains measured under flash condi-tions. In writing Eq. (10) it has been assumed that the grain size at zero time is much smaller than at the times where the equation is as-sumed to apply [Turnbull, Eq. 91][65].

The procedure is to first determine the grain size exponent, n_{il} for each of the four cases at an isothermal temperature, and then determine ΔH_{ij} from Arrhenius plots for the equation in the following form

$$\ell n\left(\frac{G_{ij}}{t^{n_{ij}}}\right) = \ell n A_{ij} - \frac{\Delta H_{ij}}{R} \cdot \frac{1}{T} \qquad (11)$$
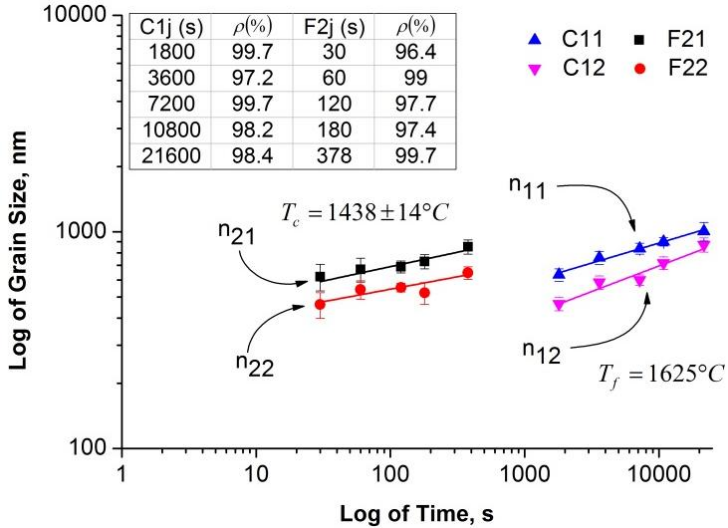
Fig. 26. Log-log plot for time exponent for grain growth for conventional sintering at 1625°C (C11= Alumina and C12 = Zirconia) and flash sintering at 100 Vcm^{-1} (F21= Alumina and F22 = Zirconia). T_f = furnace temperature and T_c = specimen temperature estimated by the black body radiation model with the emissivity values of 0.73-0.92. ρ = final density of sintered samples at different time intervals.

The grain size exponent was measured by isothermal experiments. In all instances the specimens had a density >95% prior to the measurements of grain growth. For conventional sintering the sampled were annealed at 1625 °C for up to 6 h. Grain growth under an electrical field was measured by holding the specimens in Stage III for different durations. In Stage III the specimens remain at constant temperature. It is to be noted that the flash can be triggered not only in porous samples but also in fully sintered samples. Stage III was induced in these samples by initiating the flash at 100 Vcm^{-1}, and then switching to a current limit set to 84 mAmm^{-3}, while the furnace

59

was held at a constant temperature of 1300°C. The samples were held in Stage III for periods up to 378 s. The specimen temperature in this state was calculated from the black body radiation model with emissivity values ranging from 0.73-0.92 [62], and was estimated to have been in the 1424°C-1452°C range. The results are plotted in Fig. 26. The four different values for n_{ii} obtained in this way are reported in Table 7.
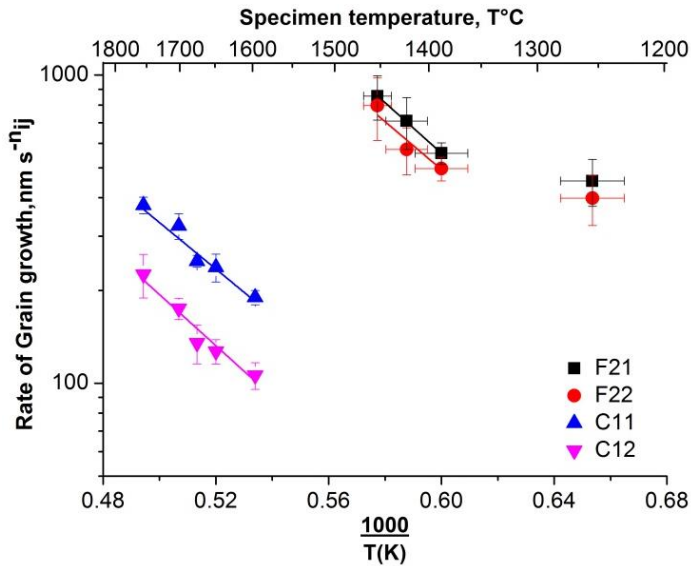
Fig. 27. The Arrhenius plot for grain growth of conventionally (C) and flash sintered (F) specimen for alumina (C11 and F21) and zirconia (C12 and F22) respectively.

An Arrhenius plot of the data according to Eq. (11) is plotted in Fig. 27. The temperature was varied for flash sintering by varying the applied field while current limit and hold time during current control was kept constant. The error bars for temperature correspond to the range of emissivity values assumed for the black body radiation

model. The data for flash and conventional sintering appear to have similar activation energy, but different intercepts on the y-axis, reflecting a significant acceleration of grain growth under flash sintering. These values are summarized in Table 6. The activation energies for grain growth for conventional and flash sintering lie in the range 142-159 kJ mol^{-1} for both alumina as well as zirconia grains. The point for 150 V cm^{-1} appears to deviate from the linear Arrhenius fit because of large dispersion of grain size at the center of the cross section. Perhaps this could be related to a high current setting leads to localization of high current at the center of the specimen.

Table 7. Time exponents, pre-exponential factor and activation energy for grain growth under conventional (Cij) and flash (Fij) sintering condition.

Grain growth parameters	Conventional sintering		Flash sintering	
	Al_2O_3	ZrO_2	Al_2O_3	ZrO_2
	ij = 11	*ij* = 12	*ij* = 21	*ij* = 22
n_{ij}	0.18	0.24	0.13	0.12
A_{ij} (nm.s$^{(-nij)}$)	0.20×10^7	0.27×10^7	4.63×10^7	2.54×10^7
ΔH_{ij} (KJ.mol^{-1})	145	159	157	150

4.1.2 Discussion

a) Comparison of Single Phase and Two-Phase Specimens

We have explored flash sintering of a two-phase ceramic, where one phase, 3YSZ, flash sinters at fields below 150 Vcm^{-1}, and the other, undoped Al$_2$O$_3$, does not exhibit flash sintering even at fields as high as 1000 V cm^{-1}.[9] A 50/50 vol% mixture of the two exhibits flash sintering at conditions similar to those used for 3YSZ. The sintered ceramics are nearly fully dense with a two-phase microstructure. Both zirconia and alumina phases exhibit grain growth at a rate that is significantly higher than in conventional sintering.

The interesting question arising from these experiments is that the sintering and grain growth kinetics of alumina in the composite are enhanced at fields where single phase alumina remains essentially immune to the effects of electric fields. In single phase alumina the matrix and the grain boundaries are constituted from alumina. The difference in the composite is that it also contains bi-phasic zirconia-alumina interfaces. Is it then to be inferred that the enhance kinetics related to alumina are related to faster diffusion of alumina along these two-phase interfaces? This remains an interesting question for the future.

Field assisted sintering occurs by at least two different mechanisms: at low fields enhanced sintering happens without the non-linearity in the conductivity, which we have called FAST sintering, and at high fields where sintering occurs suddenly and is accompanied by the non-linear conductivity, called flash. FAST sintering has been successfully explained by the reduced rate of grain growth under weak electrical fields. Flash sintering is complex involving Joule heating, and generation and transport of defects that carry both charge and mass. Therefore, there is a transition from FAST to flash

as the electric field is increased. Sometimes this transition occurs gradually, as in single phase titania and barium titanate, and sometimes abruptly as in 3YSZ. In single phase alumina, which exhibits flash sintering only when doped with MgO and at much higher fields and temperatures than 3YSZ, the transition is gradual. In the zirconia/alumina composites, the transition occurs somewhat gradually. It would seem that, in this respect, the transition is a blend of 3YSZ and alumina behaviors.

b) Joule Heating

The phenomenon of flash sintering is often, ostensibly, attributed to Joule heating. The argument that the specimen generally heats up to the extent that sintering may occur in mere seconds is likely not tenable given the extensive measurements of specimen temperature, and the good agreement found between these measurements and predictions from the black-body radiation model. The other argument is that there is local heating at the particle-particle interfaces during sintering. This argument is difficult to justify since the very high temperature differentials at the grain boundary that would be required to explain the observations may not be justified on grounds of thermal diffusion into the adjacent grain matrices, even if it is admitted that photon-trapping at the interfaces may lead to some degree of local heating at the grain boundaries. It is also well to keep in mind that the flash phenomenon is seen not only in sintering, but also in pre-sintered fully dense specimens. The sintering experiment simply highlights the point that the non-linear increase in conductivity is accompanied by a similar abrupt increase in stoichiometric self-diffusion. A word of caution: the detailed work on Joule heating has been carried out on 3YSZ. It is quite possible that the extent of Joule heating would vary from one material to another, but it seems unlikely

that it on its own can explain this new and interesting phenomenon. What is often forgotten in this discussion is that the non-linear increase in conductivity is also, by itself, a novel effect.

c) Grain Growth

Systematic study of grain growth requires that specimens be held at a constant temperature and the grain size measured as a function of time. Under flash conditions these measurements are possible in Stage III, which follows the initial onset of flash. In this stage the temperature and power dissipation in the specimen remain constant. Since the great part of densification occurs during the flash, the specimens in Stage III remain at constant density, which is close to the theoretical. By holding the specimens in Stage III grain growth can be measured as a function of time at a constant temperature.

It is in this way that we have compared grain growth kinetics under conventional and flash conditions. The grain growth of each phase is measured. The grain size exponent for isothermal growth, as well as the activation energy, for four cases: alumina and zirconia grains, each in conventional and flash conditions are reported. The interesting result is that the activation energy for all four cases remains essentially the same, about 150 kJ mol^{-1}. Activation energies for diffusion are usually attributed to the energy barrier for defect mobility since the defect concentrations are usually extrinsically determined. Since the activation energy is not affected, it is reasonable to infer that the mobility of defects does not change under electric fields. We determine that the absolute rates of grain growth are much greater with than without electric fields. A possible implication is that the defect concentration is greatly enhanced by electrical fields under flash conditions.

4.1.3 Summary

Undoped alumina, which resists flash sintering at fields up to 1000 V cm^{-1} [3], exhibits this behavior at low fields when combined with yttria stabilized zirconia in a 50/50 vol% two-phase mixture. The sintering behavior of the composite lies close to the flash behavior of single-phase YSZ.

Field assisted sintering occurs by at least two different mechanisms. At low fields it is enhanced without the non-linear increase in conductivity. This behavior, called FAST, is satisfactorily explained by the reduced rate of grain growth under weak electrical fields. At higher fields sintering occurs quickly as if in a flash and is accompanied by non-linear conductivity. The transition from one to the other can be abrupt or gradual. In the composites the transition occurs gradually as the field strength is increased. Indeed in the intermediate regime, sintering occurs at first in the FAST mode and then transitions to a flash.

Flash sintering behavior falls into three stages, pre-flash, Stage I, the transition, Stage II, and post flash, Stage III. The majority of accelerated sintering takes place in Stage II. The sample remains in a high conductive but stable state of Joule heating in Stage III. In this stage, when the samples are close to full density, grain growth can be measured under isothermal conditions, and compared with grain growth under conventional conditions. We report that grain growth is greatly enhanced in Stage III, although the activation energy for grain growth remains nearly equal to that in conventional behavior. The higher rate of grain growth is attributed to enhanced defect concentration. The results suggest interesting effects of electric field on defect kinetics at bi-phasic grain boundaries.

4.2 Isothermal flash sintering

Among the various mechanisms proposed in the literature, Joule heating remains of the greatest interest [13,14], although the temperatures required for nearly instantaneous sintering are far above what can be reasonably well predicted from Joule heating. While the increase in specimen temperature certainly plays a role in the sintering phenomenon, it, by itself is not sufficient to explain this unusual phenomenon.

The other suggestion has been to say that a defect avalanche in the form of Frenkel pairs is precipitated which ionize into charge neutral defects and electron-hole pairs. The defects enhance diffusion while the e-h pairs induce high conductivity and photoemission [15]. While, this suggestion does explain why diffusion, conductivity and photoemission are simultaneously enhanced, a quantitative understanding of how it can happen remains obscure. Some support for the defect induced mechanism is found in residual effects of the flash on defect concentrations in MgO-doped alumina [4] and in yttria stabilized zirconia [16].

The flash phenomenon is present in porous as well as fully sintered specimens. In pre-sintered samples the flash is manifested by a non-linear increase in electrical conductivity and quite intense photoemission. In porous samples the onset of high rates of sintering highlights that conductivity and photoemission is also accompanied by a huge increase in self diffusivity.

If indeed flash sintering is instigated by the "nucleation" of defects, then it should be accompanied by an incubation time in experiments carried out at isothermal furnace temperatures. Here we report these results, and show that they are related very non-linearly to the applied field. Tentatively, a model for the nucleation of dipole

clusters, of abnormally large permittivity, is developed and analyzed to explain these results.

4.2.1 Results

A typical specimen response to the applied electric field is given in Fig. 28. In this experiment the furnace temperature was set to 1275°C, the sample was held at this temperature for 30 min, at which point an electric field of 75 V cm^{-1} was applied. The time shown in Fig. 28 is from the moment of the application of the field. After incubation time of 234 s specimen shows the abrupt rise in shrinkage and conductivity. The power supply is then switched to current control with the limit set to 85 mA mm^{-2}. The flash condition was maintained for 60 s in current control at which point the field was switched off. The power density, equal to the product of the field and the current density, quickly rises to a peak, and then declines as the conductivity of the specimen continues to increase, eventually settling to a steady state, at a field of 50 Vcm^{-1}.
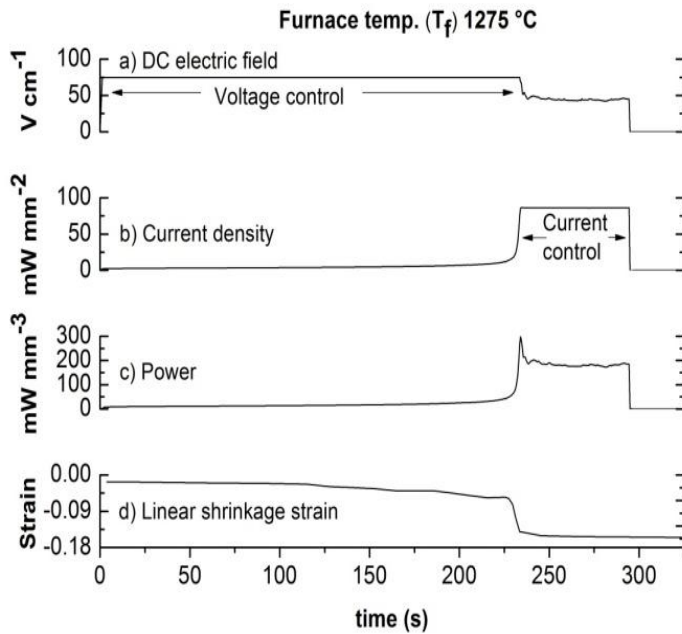
Fig.28. Isothermal flash sintering verses time curves for a) DC electric field, b) current density, c) power and d) linear shrinkage strain at 1275°C for 75 V cm^{-1}.
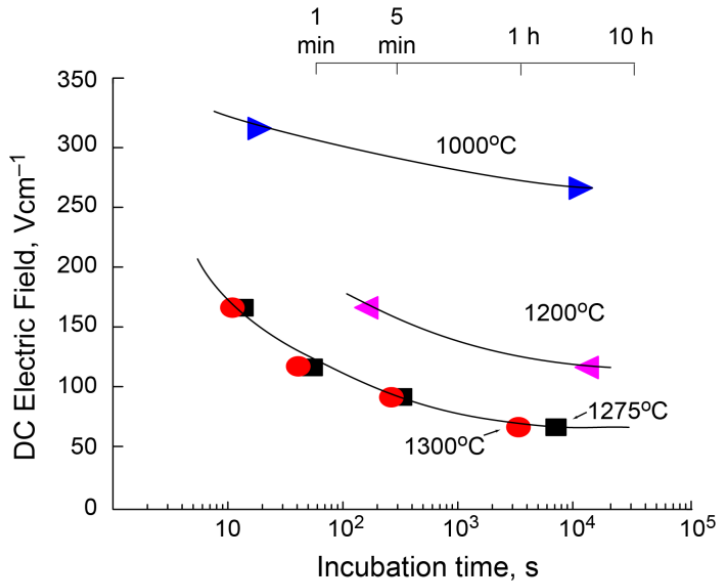
Fig. 29. Effect of DC electric field on the onset of flash sintering at different isothermal furnace temperature (1000°C, 1200°C, 1275°C and 1300°C) in a) liner b) semi-log diagrams .

The purpose of these experiments was to measure the change in the incubation time for the onset of the flash as a function of the electric field and the furnace temperature. These results are reported in Fig. 29. At a given temperature the incubation time lengthens non-linearly, even on a logarithmic time scale, as the applied field is decreased, suggesting that the electric field serves as the driving force for the nucleation event. As the temperature is lowered, a higher field is required to instill the flash. The rationale for this behavior is that the incubation time, being associated with the growth of an embryo of a critical size, depends on the size of the critical embryo and the time required for it to grow to the critical size which de-

pends on diffusivity. If the diffusivity is reduced (by lowering the temperature) then the critical size of the nucleus must be smaller. Since the critical embryo size is inversely proportional to the driving force, a smaller nucleus size requires a greater driving force, that is, a higher electric field.

The microstructures obtained in these experiments were the same as obtained in constant heating rate experiments as described in section 4.1 [17]. The size of alumina and zirconia grains was measured for experiments carried out at furnace temperature of 1275°C under different levels of applied field. A typical microstructure taken different applied field is shown in Fig. 30. The grain sizes for alumina and zirconia grains at 50 Vcm^{-1}, were 693 ± 69 nm, and 684 ± 59 nm. At 73 Vcm^{-1} they were 671 ± 62 nm and 612 ± 10 nm respectively. At 100 Vcm^{-1}, 758 ± 118 and 645 ± 40 nm, and at 150 Vcm^{-1}, 727 ± 151 and 675 ± 68 nm respectively for alumina and zirconia grains. The specimen temperatures estimated from black body radiation model, using emissivity values in the range 0.73 to 0.92, were 1389-1415°C, 1394-1421°C, 1421-1453°C and 1424-1458°C, at fields of 50, 75, 100 and 150 Vcm-1. The detailed estimation of specimen temperature is discussed in the previous section (4.1). The densities of these specimens, given at increasing electrical fields were 94.4%, 97.1%, 98.8% and 98%, respectively
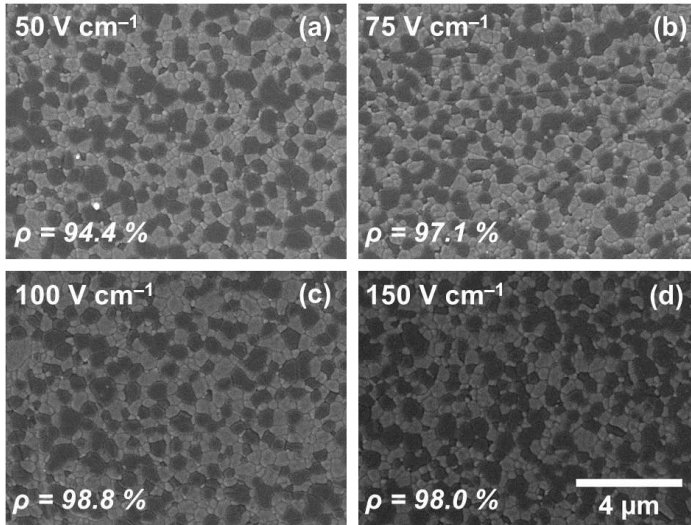
Fig. 30: Micrograph of the grain size obtained from isothermal flash sintering at 1275°C. ρ represent the relative density obtained by Archimedes method.

4.2.2 A model for nucleation

In isothermal furnace temperature experiments, the flash phenomenon occurs in three stages. The first is the onset of the non-linear conductivity at the applied field. This is the nucleation event, which occurs at the furnace temperature, and embodies an incubation time. The non-linear rise in conductivity is controlled by switching the power supply to current control; this is the second stage. The third stage is the quasi-steady state that is established under current control. Joule heating begins in Stage II and continues in Stage III. Thus flash sintering has two unusual features: (i) the nucleation of the non-linear event, and (ii) and the rapid rate of sintering in the highly conducting state of Stages II and III. Much of the community's (and our)

focus has been on the high sintering rates in these later stages, where Joule heating does indeed occur and whose overall role in the process remains controversial. However, the peculiar nucleation of the non-linear transition from insulating to conducting state, which occurs at the furnace temperature, has so far been often overlooked. This paper is concerned with this nucleation event, which precedes Joule heating. It occurs at furnace temperature.

Thermal ionization of interstitials and vacancies above a critical electric field, as analyzed in the Poole-Frenkel model [67,68], could also explain the flash phenomenon. However, substitution of numbers shows that the fields required for Poole-Frenkel ionization would have to be several orders of magnitude greater than employed in the flash experiments. In any event the Poole-Frenkel approach does not invoke a nucleation like behavior, where embryos grow with time to a critical state, as the underlying process.

The incubation time for nucleation that varies highly non-linearly with driving force is well known in phase transformations in the solid state. The phenomenon has been discussed under the title of transient nucleation in the early work of Turnbull [69,70]. The embryo grows slowly gathering the atoms of a minority species in the solid-solution, competes with the dissolution of the embryo, until it reaches a supercritical size.

The following analysis is based upon these early concepts. We hypothesize that an embryo of high dielectric constant is formed under the influence of the electric field. The high dielectric constant is assumed, rather elementarily, to arise from the aggregation of aligned dipoles made of the vacancy-interstitial Frenkel pairs. It is relevant that very high relative dielectric constants, referred to as colossal permittivity have been discussed in barium titanate when the grain size is of nanoscale dimensions [71]. Values as high as 10^6 have been reported [72]. In at least one instance permittivity of $3*10^5$ in

72

large grained (several hundred nm) barium titanate prepared by microwave sintering has been reported [73]. In the nucleation phenomenon we are concerned with embryos just a few nm in diameter, much smaller than the grain size where these collossal permitivities have been measured. Phenomenologically it appears that a smaller dimension leads to a higher permittivity. Therefore, the assumption that the embryos have permittivity at least in the 10^5-10^6 range is justifiable. We expect that this point will remain of interest in future studies of this nucleation phenomenon.

The driving force for nucleation arises from the polarization energy of this aggregate of a high dielectric constant. This energy, per unit volume, ΔG_V, is given by

$$\Delta G_V = \frac{1}{2}\varepsilon_o \varepsilon_E E_j^2 \qquad (12)$$

Where ε_o is the permittivity of vacuum, ε_E is the dielectric constant of the embryo, and E_j is the applied electric field.

The growth of the embryo is opposed by the energy of the interface it forms with the parent lattice, which we call γ_E. The total free energy of the embryo, relative to the zero field state, is then given by

$$\Delta G = -\frac{4}{3}\pi r^3 \Delta G_V + 4\pi r^2 \gamma_E \qquad (13)$$

Equation (10) reaches a maximum, the critical state, when

$$\left(\frac{\partial \Delta G}{\partial r} = 0 \right)_{r=r^*} \qquad (14)$$

Substituting Eq. (13) into (14), and then putting back the value for $r*$ so obtained into Eq. (13) to obtain the following relationships

73

$$r^* = \frac{2\gamma_E}{\Delta G_V} \quad , \qquad (15)$$

and

$$\Delta G^* = \frac{1}{2}\left(\frac{4\pi}{3}r^{*3}\right)\Delta G_V, \quad \text{or} \quad \Delta G^* = \frac{128\pi}{3}\frac{\gamma_E^3}{\varepsilon_o^2\varepsilon_E^2 E_j^4} \qquad (16)$$

where ΔG^* is the free energy barrier expressed at the critical state of the embryo. Substituting Eq. (12) into (15), gives

$$r^* = \frac{4\gamma_E}{\varepsilon_o\varepsilon_E E_j^2} \qquad (17)$$

The incubation time, which is the time required to grow the embryo slowly uphill towards a critical size, increases highly non-linearly with the number of atom-species in the critical nucleus [70]. It depends on the mobility of the species in the region surrounding the embryo. Typically a critical size of a few tens of nanometers is realizable within the laboratory time scale at elevated temperatures, where solid state diffusion phenomena, such as ionic condutivity, occur at measureable rates. Thus the size of the critical nucleus becomes a measure of the incubation time for reaching the supercritical state.

We consider the size of r^* estimated from Eq. (17). Although the local field within the material may be enhanced by inhomogenieties, to a first approximation we may set E_j equal to the applied field, keeping in mind that this would be the lower bound for the driving force for nucleation. The interfacial energy γ_E is likely to be very low since the embryo will be coherent with the parent matrix, its magnitude arising from the energy of the dipoles at the surface relative to those within the embryo. There is an equivalence with the energy of the domain walls in ferroelectric crystals formed between regions of opposite (or orthogonal) polarizations. These walls can be

74

several atom layers wide. Their energy is calculated to be 1-10 m Jm$^-$^{2} [74]. In the present cast the energy is likely to be considerably lower since the dipoles only within the embryo, and the interface can be expected to be sharp. We shall assume that $\gamma_E = 1 \text{mJm}^{-2}$, recognizing well that future discussions of the nucleation mechanism are likely to center on the atomic and electronic structure and its relationship to energy and kinetics of the embryo-matrix interface [75].

It remains to consider a value for the dielectric constant. With a high density of charges dipoles it is expected to be very high, and we assume it to lie in the range $\varepsilon_E = 10^5 - 10^6$, as discussed above [71,72]. The physical constant $\varepsilon_o = 8.85 * 10^{-12}$ Fm^{-1}. The estimates of $r*$ calculated in this manner are given in Table 8. The values for the embryo size for the assumed values of the interfacial energy and dielectric constant are within the bounds of experimental results.

A major uncertainty in the analysis is the assumption of the local field at the embryo being equal to the applied field. In fact inhomogenieties in the microstructure, such as grain boundaries and dislocations can intensify the local field. Since the embryo size varies inversely as the square of the field, a high value, locally, can substantially reduce the barrier to nucleation.

Table 8. Estimates of the critical embryo radius from Eq. (17).

E_j , Vcm^{-1}	e_E	g_E, mJm^{-2}	$r*$, nm
1000	10^6	1	45
3000	10^6	1	5
1000	10^6	10	450
3000	10^6	10	50

Another way of analyzing the nucleation phenomenon is to calculate the probability of nucleation , p_E , then given by

$$p_E = \exp\left(-\frac{\Delta G^*}{k_B T}\right) \qquad (18)$$

Substituting from Eq. (16) leads to the plots shown in Fig. 31 (for T=1000 K, and $\varepsilon_E = 10^6$). The plots show the highly nonlinear increase in p_E with E_j, for three values of γ_E. The threshold value for the nucleating field can be estimated from the asymptotes to the curves. The steepness of the curves, especially in view of the logarithmic scale for p_E is characteristic of a nucleation phenomenon.
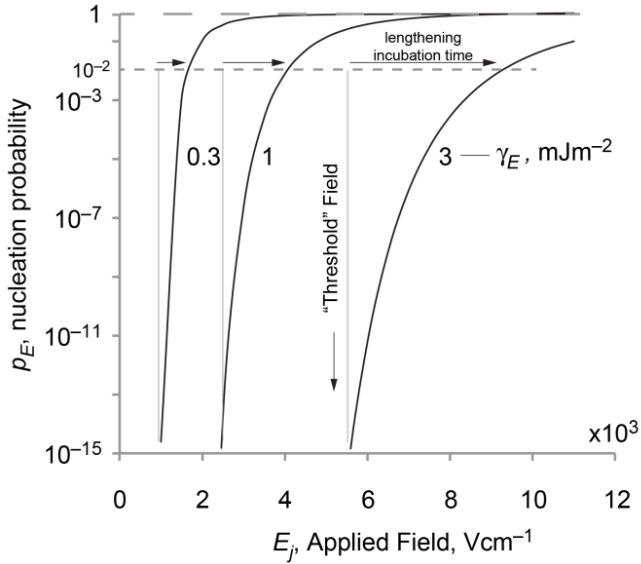
Figure 31: Plots for the probablity of nucleation as a function of the interfacial energy. T =1000 K, and ε_E = $10^{6.}$

4.2.4. Summary

The phenomenon of flash sintering has the characteristics of nucleation and growth. It occurs abruptly, above a threshold field as the temperature of the specimen is raised at constant rate. The incubation time which varies with the applied field at a constant furnace temperature, confirms that the electrical field is the driving force for the nucleation mechanism. Nucleation phenomena are defined by a volumetric driving force which favors the event, and the interfacial energy which opposes it. The surface to volume ratio of the embryo determines the probability of nucleation and the incubation time to

77

reach a nucleus of a critical size. The analysis presented above assumes that the polarization energy of the embryo is the driving force for nucleation.

If the hypothesis is correct, then the issue of the interface between the embryo and the matrix gains great scientific significance. Since the interface is not only important in its energy, but also in how it produces an avalance of defects, once a supercritical state is reached. These questions of interfacial polarization and generation of electrons and holes is being studied in ab-initio calculations of hetero-interfaces [75]. There however, the creation of the "electron gas" is postulated to remain localized near the interface. The new question in the context of flash sintering is that the electron gas spreads through the specimen inducing the entire specimen to become electronically conducting. In addition to the energy and the atomic structure of the interface, the dielectric constant of the embryo, which determines the polarization energy, is a critical parameter in the nucleation model. We postulate the embryo to consist of aligned dipoles, much like in ferroelectric ceramics. Values of permittivity in the 10^5-10^6 range yield plausible values for the critical size of the embryos. Both these parameters, interface structure and polarization of the embryos, will remain of fundamental interest in further studies of why there is the abrupt transition from the insulating to the conducting state. Why this transition is followed by ultrahigh rates of self-diffusion is a further mystery in flash sintering.

It is worthwhile to keep in mind that nucleation occurs at the furnace temperature. Joule heating is a consequence of the nucleation of the flash event. It cannot be its cause.

4.3 Effect of alumina addition on flash sintering of 3YSZ/Al$_2$O$_3$ composite

4.3.1 Results and discussion

Influence of alumina addition on flash sintering of composite, from both constant heating rate as well as isothermal flash sintering are shown in Fig.32 and Fig.33. In CHR experiments (Fig.32), the power versus temperature is plotted with respect to alumina addition. The flash sintering is observed with sudden rise in power of the specimen at a threshold temperature. For a 10 vol% of alumina, the flash was noticed at 900°C. Note that the temperature mentioned is of furnace temperature and not the specimen temperature (which was much higher than furnace temperature during stage III). As we increase alumina addition to 20, 30, 40 and 50 vol% the flash sintering temperature increases to 925°C, 1013°C, 1090°C and 1216°C. These suggest addition of alumina increases the resistivity by increases the insulating boundaries of alumina [76].

On the other hand, in case of isothermal flash sintering. The power versus incubation time is plotted with respect to alumina volume percent (Fig.33). Similar effect was observed with alumina addition as seen for CHR experiment, but here it occurs with incubation time. These suggest that modification of the grain boundaries will have higher influence on the flash sintering.
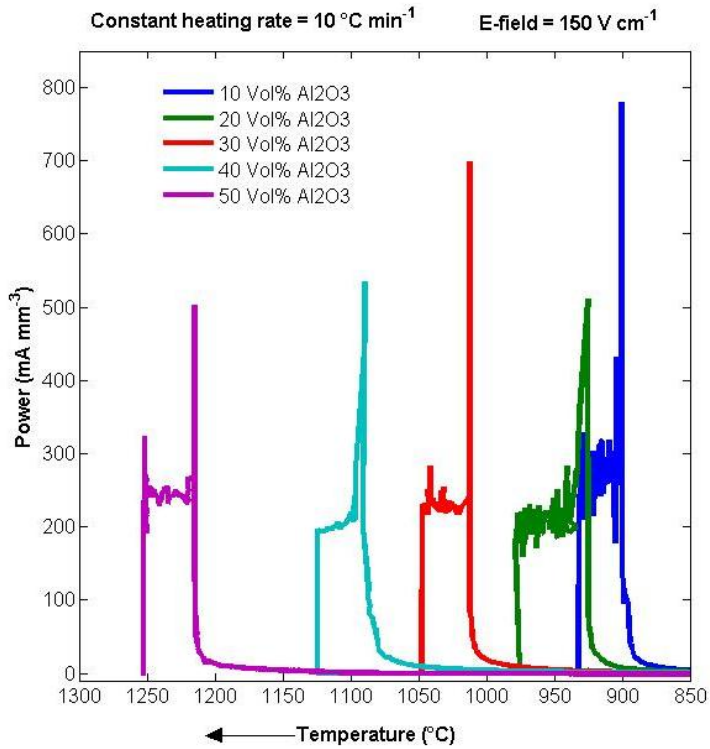
Fig.32. CHR flash sintering for varying concentration of alumina (10, 20, 30, 40 and 50 vol%) in 3YSZ/alumina composite at 150 V cm^{-1}.
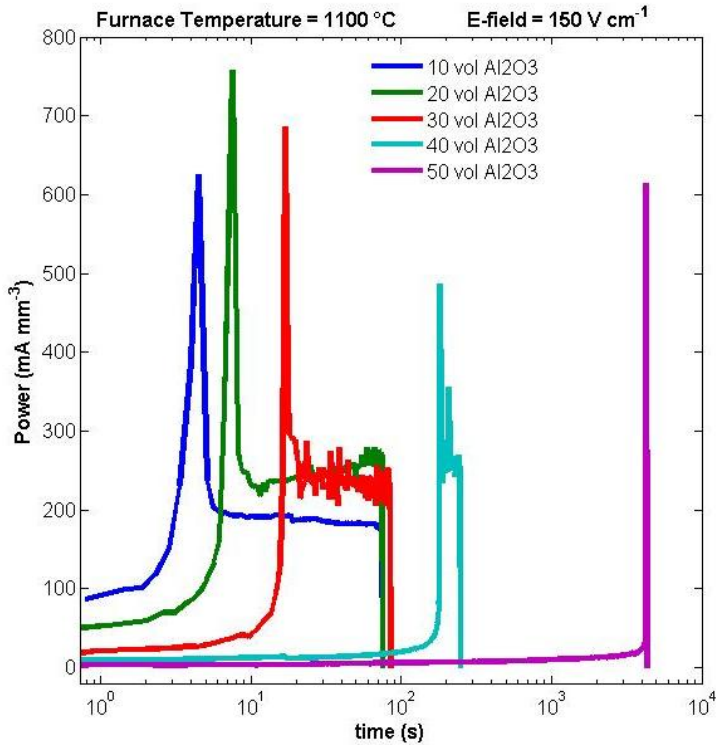
Fig.33. Isothermal flash sintering at 1100°C for varying concentration of alumina (10, 20, 30, 40 and 50 vol%) in 3YSZ/alumina composite at 150 V cm^{-1}.

The density along with the flash sintering furnace temperature was shown in table 9. The Archimedes density obtained for all the flash sintering samples were more than 95 %. From the XRD analysis (Fig. 34), the peak related to each phases were present. Also the peak were stable without peak shift, suggest the limited solubility of two phases in the composite matrix.
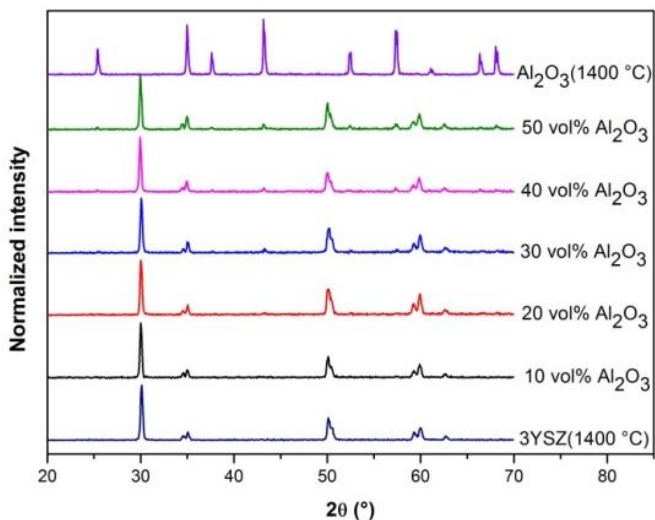
Fig. 34. XRD pattern of the $3YSZ/Al_2O_3$ composite.

Table 9. The onset of flash temperature and incubation time along with Archimedes density for alumina addition on composite.

Alumina concentration, Vol. %	Flash temperature (CHR), °C	Incubation time for flash (ISO), s	Relative density (CHR), g cm⁻³	Relative density (ISO), g cm⁻³
10	900	4	98.9	96.4
20	925	8	97.8	98.7
30	1013	17	98.0	99.8
40	1090	182	99.7	99.1
50	1216	4260	97.6	96.1

The thermally etched flash sintered microstructures at 150 V cm⁻¹ for isothermal temperature of 1100°C are shown in Fig. 35(a-e), for $Al_2O_3/3YSZ$ composite containing 10, 20, 30, 40 and 50 volume

82

fraction of Al_2O_3. The two phases of composite can be clearly identified from differences in its colour, the dark one represents alumina while the bright one for zirconia. The grain sized distribution for each phases were shown in Fig. 36.

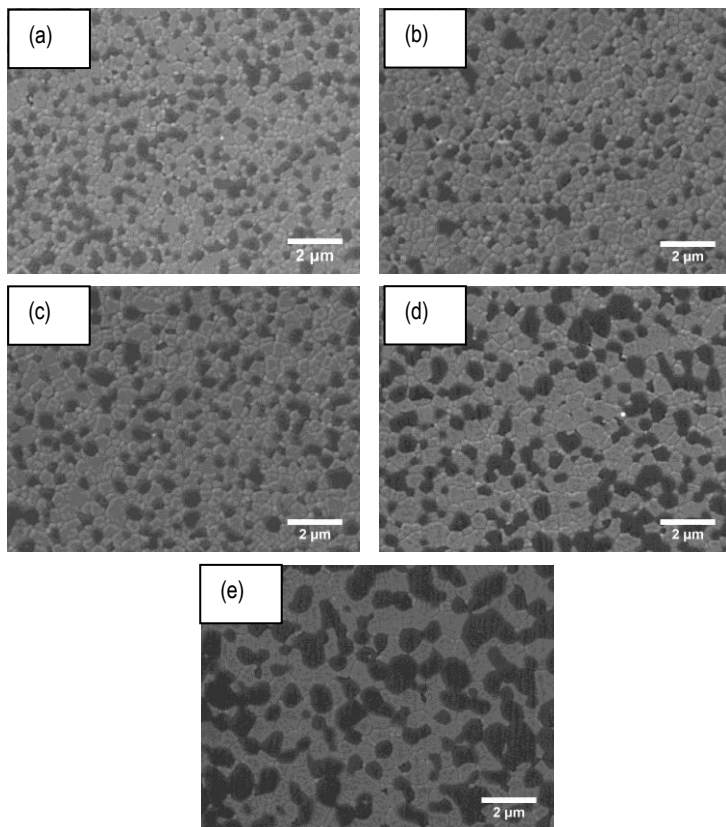Fig. 35 Micrograph obtained after flash sintering of the Al_2O_3/3YSZ composite at 150 V cm^{-1} with different volume percent of alumina at isothermal furnace temperature of 1100 °C. (a) 10 vol%, (b) 20 vol%, (c) 30 vol%, (d) 40vol% and (e) 50 vol% Al_2O_3.

(a) 10 Vol% Al₂O₃ in Al₂O₃/3YSZ composite
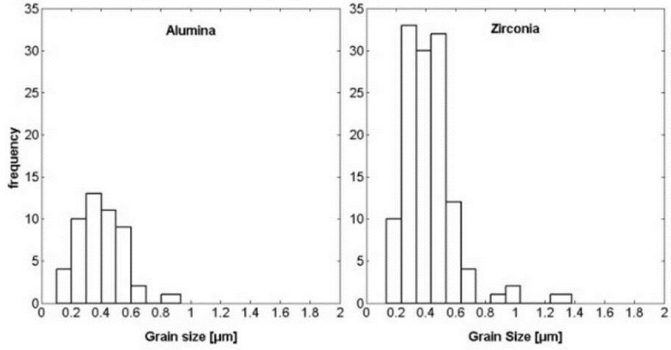
(b) 20 Vol% Al₂O₃ in Al₂O₃/3YSZ composite
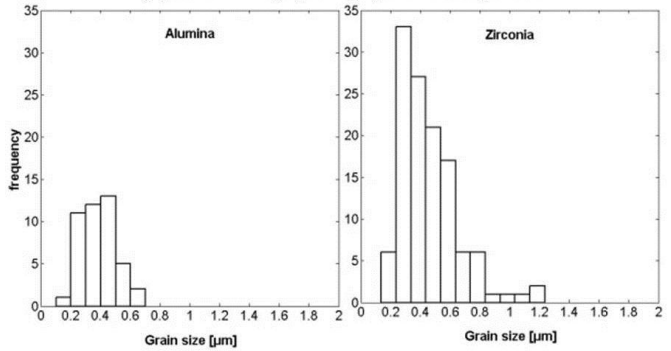
(c) 30 Vol% Al₂O₃ in Al₂O₃/3YSZ composite
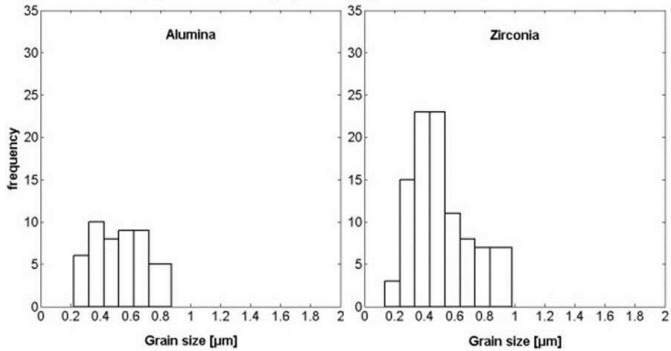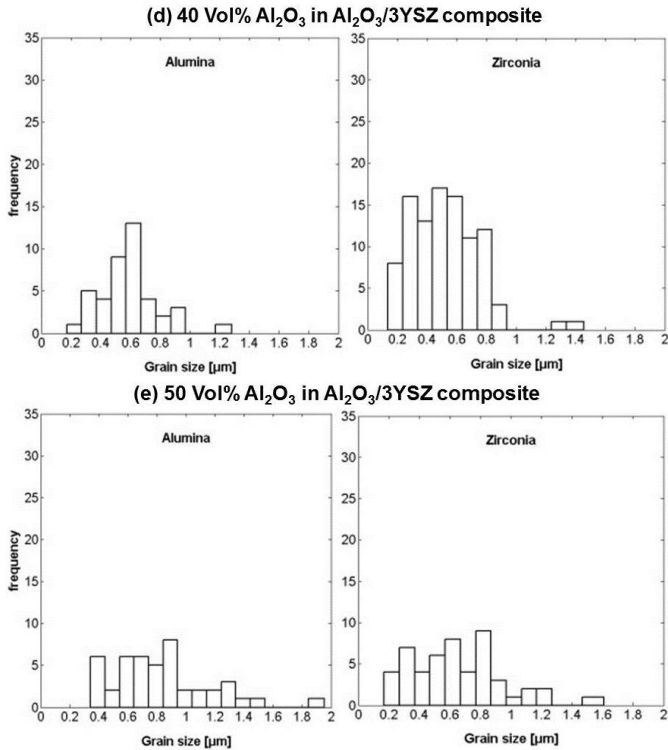
Fig. 36. histogram distribution of grain size for the above (Fig. 35) micrographs.

The average grain size of alumina and zirconia obtained were plotted with respect to volume concentration of alumina (Fig. 37). The average grain size is plotted for both the sintering condition that is (CHR and isothermal). The grain size obtained shows higher grain size of zirconia than alumina below 30 vol% alumina. At 30 vol % the average grain size in both the phase remains constant. When alumina exceeds 30 vol %, the grain size alumina grows much faster than zirconia grains.
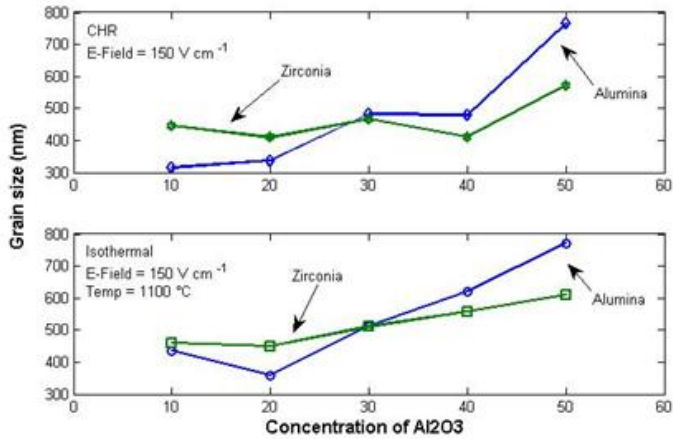
Fig. 37 The grain size with different volume fraction of Al_2O_3 in Al_2O_3/3YSZ composite.

4.3.2 Conclusions

Addition of alumina increases the onset for the flash sintering. Higher the alumina contained higher will be the onset temperature (CHR) or incubation time (ISO). Below 30 vol% of alumina, the diffusivity of zirconia was much faster compare to alumina. However, above 30 vol% of alumina, diffusivity of alumina is more mobile in contrast to zirconia grains.

4.4 Preliminary Results on Flash Sintering of Hydroxyapatite (HA)

4.4.1 Results and Discussion

a) Field assisted sintering

The Sintering of ceramics leading to densification occurs as sample temperature rises which is accompanied by shrinkage. If we apply electric field to the sample, sintering is enhanced and occurs at lower temperature as shown in Fig. 38. The sintering nature of two different hydroxyapatite powders are shown here. Fig.38a represent for HA-A and Fig. 38b represents for HA-B. . The conventional sintering curve represented by 0 V shows different sintering profile for the two HA samples, but shares a common onset temperature of ~700°C.

Field assisted sintering is divided into two regimes, the FAST and the flash regime. In the FAST regime, the sintering occurs with gradual enhancement of shrinkage while in the flash regime sintering accompanied by sudden shrinkage. At 500 V cm^{-1} both HA samples undergo FAST sintering; the densification was enhanced at ~950°C which continues until 1317°C with small a flash at the end where strain remains almost constant.t. As field is increased to 1000 V cm^{-1} the sintering clearly divides into two regimes. Initially it undergoes FAST sintering and then transits into flash with vertical slop in its shrinkage strain curve. The two sample shows flash sintering at 1060°C and 1030°C for HA-A and HA-B respectively. This type of behaviour is known as Hybrid sintering. Similar behaviour was observed in MgO doped alumina [9], titania [43], alumina zirconia composite [58] and undoped Yttria [45].
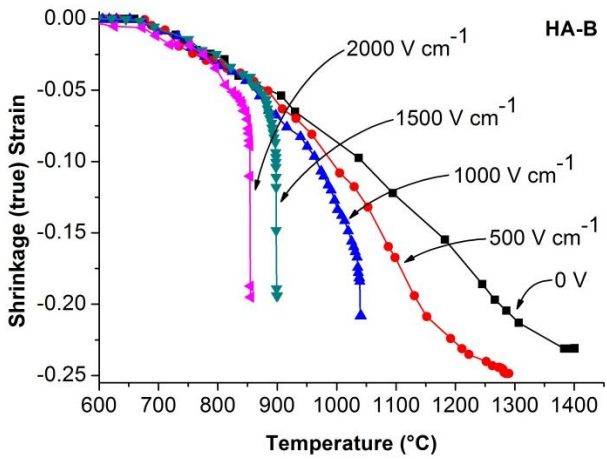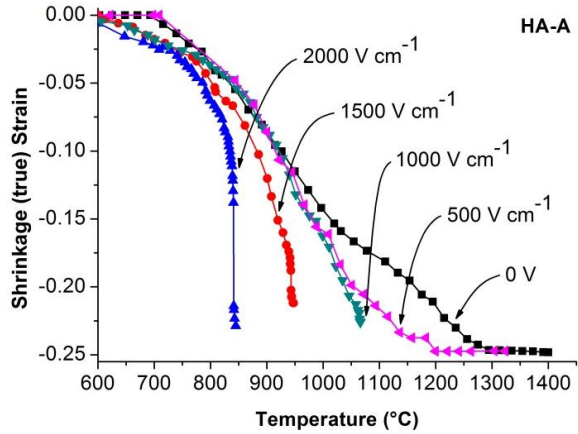
Fig. 38 Shrinkage strain for different applied electric field as a function of furnace temperature (a) HA-A and (b) HA-B

At higher field of 1500 V cm^{-1} the flash sintering tempera-

ture is reduced to 940°C and 894°C for HA-A and HA-B respectively. Finally the flash sintering temperature is further reduced to 840°C (HA-A) and 850°C (HA-B) for applied field of 2000 V cm^{-1}.

b) Joule Heating
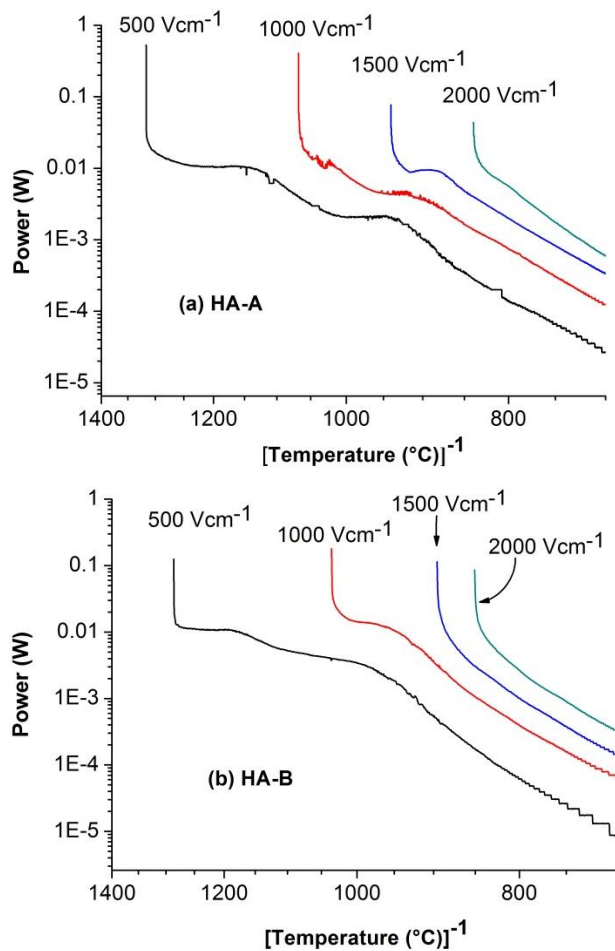
Fig. 39 Arrhenius plot of power as a function of furnace temperature at different applied electric fields (a) HA-A and (b) HA-B

In the method of flash sintering, shrinkage is accompanied by power surge in the specimen. Fig.39a and Fig.39b depicts the power runaway in the case of HA-A and HA-B at different applied field. The power is given as the product of electric field and current density. In an Arrhenius plot (Fig. 39), under applied field of 500 V cm^{-1} the current density increases linearly up to ~940°C (Fig. 39a) and ~980°C (Fig. 39b), remains stable for a while, and then again increases up to ~1130 °C and ~1190 °C respectively. After that it again becomes stable for a while and then increases abruptly. Once the current runaway occurs the power supply was switched off. For applied field of 1000 V cm^{-1} and 1500 V cm^{-1}, stable state of current density before flash, seen only above 900°C. The flash sintered sample below 900°C does not show this behaviour. The stability of the power before flash could be related to its electrical conductivity.

c) Micrograph

The microstructures obtained after consolidation, either by flash or by conventional sintering are demonstrated in Fig. 40-41. The fractured surface of the samples obtained by conventional sintering shows higher grain size compared to that of flash sintered sample. Both the HA samples obtained by conventional sintering shows similar microstructure. The microstructure of the samples sintered with 500 V cm^{-1} is different from those sintered at higher fields (1000-2000 V cm^{-1}). At a respective voltage, the grain size of flash sintered HA-B is much smaller than that of HA-A. The difference in grain size could be related to the initial particle morphology which was different for both the powders (Fig.16).
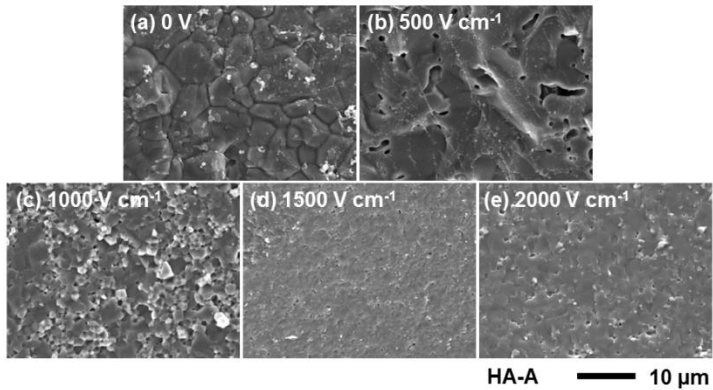
Fig. 40 Micrograph obtained after consolidation at different applied electric field for HA-A.
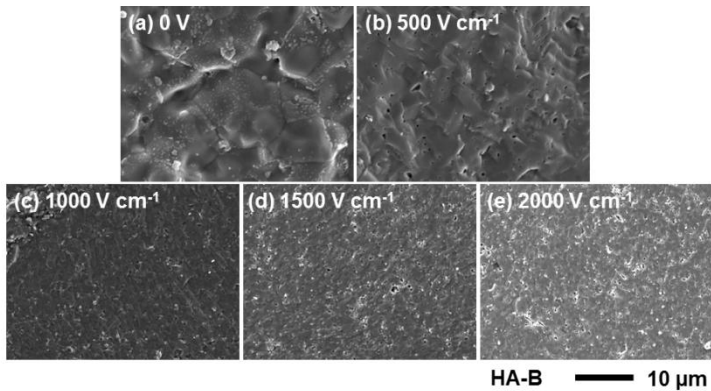
Fig. 41 Micrograph obtained after consolidation at different applied electric field for HA-B.

The final density of the sintered sample were analysed by Archimedes method and are reported along with the furnace temperature in table 10. The relative densities obtained are in the range of 90-95 %. The variation in the density with applied electric field

could be due to uneven final current density during flash sintering.

Table 10. Archimedes density and furnace temperature for both hydroxyapatite samples

Electric field $(V\ cm^{-1})$	HA-A		HA-B	
	Relative density (%)	Furnace temperature (°C)	Relative density (%)	Furnace temperature (°C)
0	96	1400	91	1400
500	94	1317	93	1287
1000	93	1067	90	1035
1500	95	941	90	896
2000	92	840	95	850

d) X-ray analysis and FTIR

XRD patterns of as received powder and flash sintered hydroxyapatite at electric field from 0 V to 2000 V cm^{-1} are presented in Figure 42 (HA-A) and 43 (HA-B). For as received sample and sample sintered at 0 V, the spectra accounted for hydroxyapatite (HA), hexagonal crystal structure (JCPDS file 09-0432). In all the sintered samples, no additional peaks or peak shift is observed. This suggests there is no phase change of HA. However, for an applied field of 500 V cm^{-1} (Fig. 42), the relative peak intensities of HA-A was found to symmetrically depart from those given in the JCPDS file, suggesting a preferred orientation effect after flash sintering. Preferred orientation was evident for the peak intensities at 2θ=26° (002), at 2θ=31.7 (211), at 2θ=32.2 (112), at 2θ=32.9 (300) and at 2θ=53.2 (004). No

preferred orientation was observed for HA sample sintered with 0 V at 1400°C.

Preferred orientation is more evident in hydroxyapatite when sintered under applied field. The effect was reported during spark plasma sintering of HA [77]. Even during pressure assisted sintering of HA, this phenomena was observed [24]. For HA with hexagonal crystal structure, all the OH^- are known to align along the c-axis and direction of H-O or O-H are parallel to c-axis [78]. Conduction of proton is proposed to be the mechanism for enhance conductivity in HA, in which protons were transferred along the OH^- chain [79]. As a consequence of proton transfer, the defect are generated which will direct the diffusion process along the c-axis. Any change in the relative intensities for 002 and 004 plains predicts growth along the c-axis [80]. In Fig. 42, it is observed that the 002 and 004 peak intensity decreases with increase in electric field from 500 to 2000 V cm^{-1}, and at 2000 V cm^{-1} the peak intensities are almost identical to that of 0 V. It should be noted that (table 10) the temperature required for sintering decreases with the increased in applied electric field. The diffusion of ions is thermally activated process and is more active at high temperatures. Thus the samples sintered with lower electric field requiring higher sintering temperature shows enhanced preferred orientation due to higher diffusivity along c-axis. Similar effect was observed in HA-B (Fig.43), but to a lower extend compared to HA-A (Fig.42).
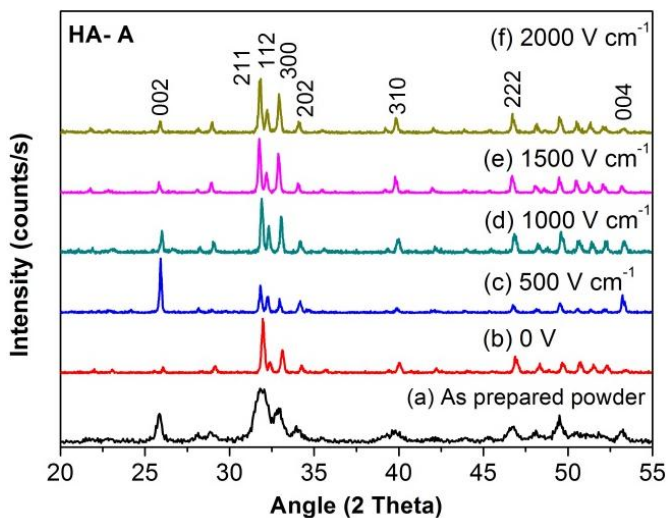
Fig. 42. XRD patterns of HA-A for as received powder, sintered at 0 V and flash sintered at different applied field: 500 to 2000 V cm^{-1}.
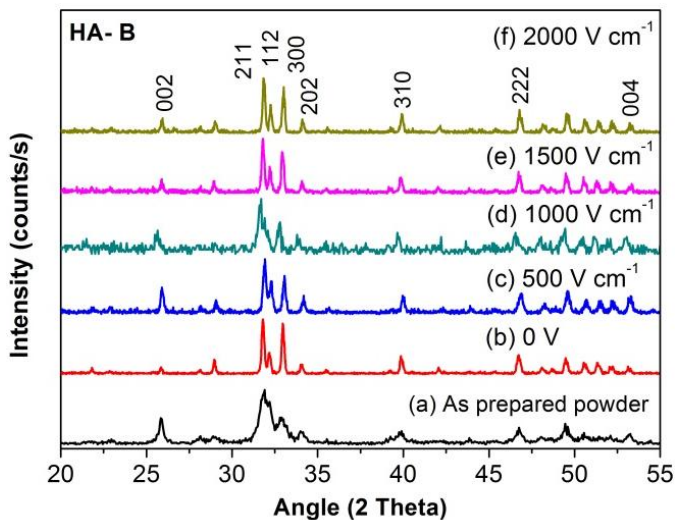
Fig. 43. XRD patterns of HA-B for as received powder, sintered at 0 V and flash sintered at different applied field: 500 to 2000 V cm^{-1}.
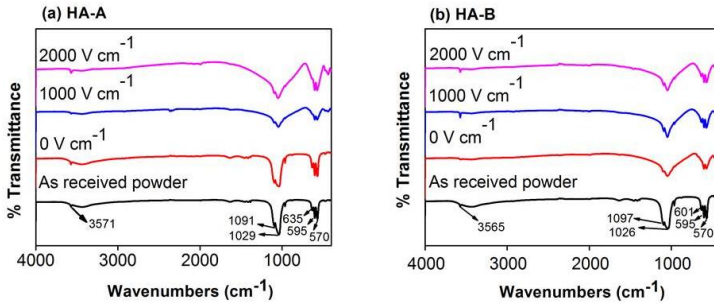
Fig. 44. Infrared spectra of (a) HA-A and (b) HA-B at different applied electric fields.

The phase stability of flash sintered HA phase again confirmed with FT-IR analysis. The FT-IR patterns of pure and flash sintered samples (HA A and HA B) are presented in figure 44. In both the cases, the peaks at 570, 595, and 1020-1120 cm^{-1} are the vibrational modes of PO_4^{2-} groups and OH groups of apatite is at 635 and 3571 cm^{-1} for all samples. The OH vibrational peak is also obtained in very high voltage sintered samples. This means that during flash sintering the HA does not show any type of structural decomposition. Thus the flash sintering is an effective technique for the sintering of HA biomaterials.

Since these are the initial results on flash sintering of hydroxyapatite, it remains to be discussed about the effect of current density on densification and grain size. Grain growth in flash sintering occurs in post flash state which occurs by controlling the current density [5]. It was reported that maximum current density, control the densification process. Similarly the densification is also controlled by post flash stage, that is flash sintering under current control [58]. This could be the future conclusions for flash sintering of hydroxyapatite. Even reducing the initial particle size can certainly affect the grain size and also the flash sintering temperature. Nevertheless, this work

95

has initiated the flash sintering of hydroxyapatite and it is necessary to analyse the process by using the electric field in much more detailed way.

4.4.2 Conclusions

We have shown that electric field can invoke flash sintering in hydroxyapatite at certainly higher field compared to other ceramic oxides sintered by flash sintering [2,3,40]. It was found that flash sintering was observed in hydroxyapatite ceramic at field > 500 V cm^{-1}. Increasing the applied field, the temperature for the onset of flash becomes lower and lower. In the present study, flash sintering of hydroxyapatite was shown at furnace temperature of ~ 840°C for an applied field of 2000 V cm^{-1}. Phase analysis by XRD and Infrared spectra confirm the formation of hydroxyapatite without phase change. The spectrum remains almost similar to that of initial powders. Certain orientation of plane along the c-axis was observed in low field flash sintering, which could be attributed to electric field induce defect migration along c-axis. This effect was not observed at higher field where sintering occurs at much lower temperature. The grain size of flash treated sample remains quite small compared to conventional sintered sample.

4.5 Effect of dopants on flash sintering of alumina

4.5.1 Results and discussion

a) Flash sintering of alumina

The Arrhenius plot of power dissipation for undoped alumina at applied field of 1500 V cm^{-1} and 1750 V cm^{-1} are shown in Fig. 45. Undoped alumina remains inert for flash sintering at field up to 1000 V cm^{-1} [9]. Increasing field to 1500 V cm^{-1} shows flash nature at ~1330°C which exists for a short time and then diminishes. The effect of arcing between electrodes was seen as a peak with unstable power dissipation, when temperature of 1050°C was reached. With further increase in field to 1750 V cm^{-1}, flash sintering was observed at 1310°C. The Archimedes density obtained after flash sintering was 95 % and 93 % for 1500 V cm^{-1} and 1750 V cm^{-1} respectively.
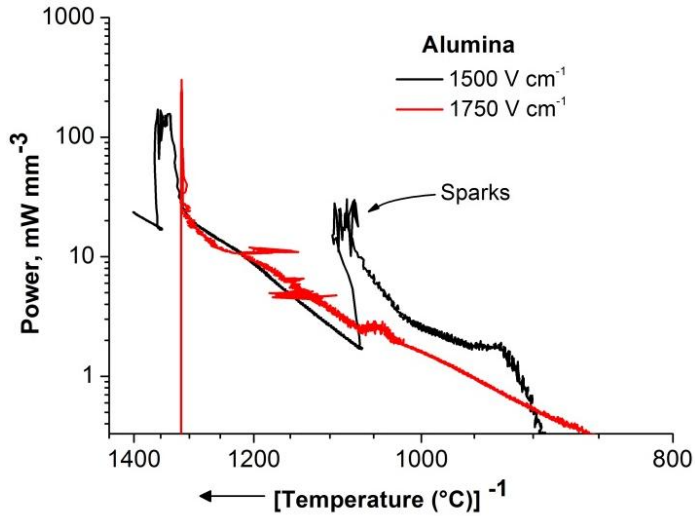
Fig. 45. Arrhenius plot for flash sintered of undoped alumina.

b) Flash sintering of doped alumina

The shrinkage strain versus temperature data for MgO and Fe$_2$O$_3$ doped alumina at an applied field of 1000 V cm^{-1}, obtained at constant heating rate of 10°C min^{-1}, are shown in Fig. 46 and Fig. 47 respectively. The shrinkage strain is observed for two different dopant concentrations: 0.5 wt% and 1.0 wt% for both MgO as well as for Fe$_2$O$_3$ doped alumina. Flash sintering is observed for both the dopant. In case of MgO doped alumina, at 1000 V cm^{-1} the shrinkage strain undergoes the same trend as that of conventional sintering (0 V). But at the onset of flash it deviates suddenly and shows vertical slop in the shrinkage strain curve. The onset of flash is observed at 1205°C (0.5 wt%) and 1215 °C (1.0 wt%).
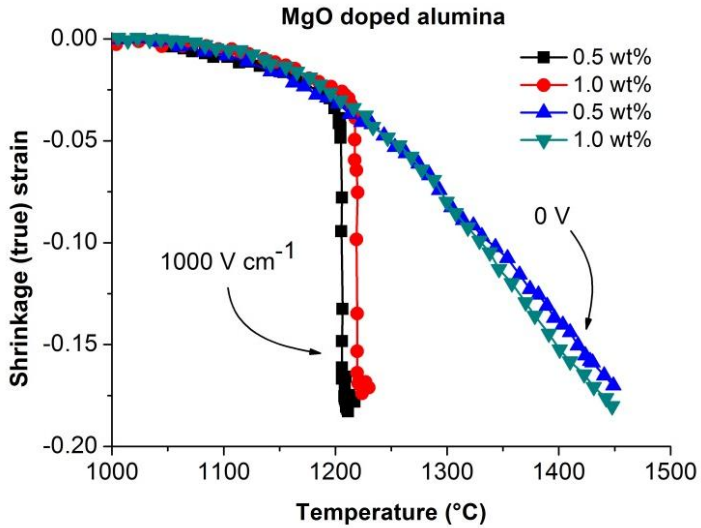
Fig. 46. the linear shrinkage strain for MgO doped alumina at 0 V and 1000 V cm^{-1}.

However, for Fe$_2$O$_3$ doped alumina, the onset of flash was seen at 1340°C (0.5 wt% and 1.0 wt%). Again the sintering curves at 1000 V cm^{-1} coincide with the conventional sintering curve, and shows similar type of deviation as that of MgO doping with vertical slope.
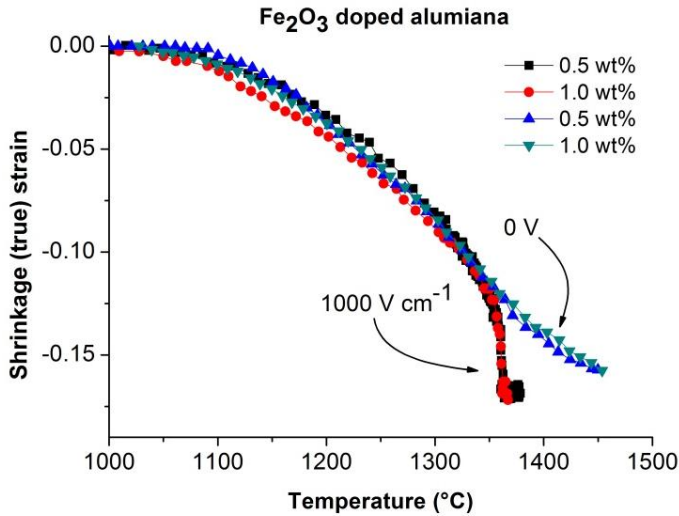
Fig. 47. the linear shrinkage strain for Fe_2O_3 doped alumina at 0 V and 1000 V cm^{-1}.

The doped–alumina exhibits a power surge at 1000 V cm^{-1} that coincides with the onset of flash-sintering. The power dissipation curves for MgO and Fe_2O_3 doped-alumina are given in Fig. 48. The power supply is then switched to current control mode in order to control joule heating. The maximum current limit available on power supply was 60 mA. It is observed that only MgO doped alumina undergoes the voltage to current mode transition, However Fe_2O_3 doped-alumina shows flash for short duration and diminishes without reaching to maximum pre-set current limit of power supply. The reason for this is unclear but it could be due to Fe_2O_3 solubility in alumina matrix [57], but XRD analysis does not show any extra peak for phase change.
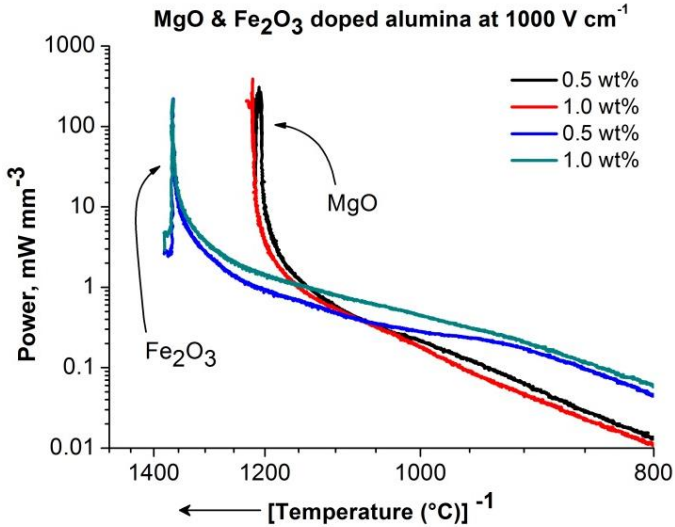
Fig. 48. Arrhenius plot of power dissipation for MgO and Fe_2O_3 doped alumina at 1000 V cm^{-1}.

The relative density obtained after consolidation either by flash or conventional sintering are shown in table 11. The densities obtained were in the range of 90-95 %. The density of conventional sintered sample was little higher then flash sintered samples. This could be due to lower current density during flash sintering. Since the power supply was limited to maximum current limit of 60 mA.

Table 11. The Archimedes density for doped alumina at 0 V and 1000 V cm^{-1}.

Dopant Concentration (wt %)	Relative density (%)			
	MgO doped alumina		Fe$_2$O$_3$ doped alumina	
	0 V	1000 V cm^{-1}	0 V	1000 V cm^{-1}
0.5	94	91	94	92
1.0	95	92	94	94

4.5.2 Summary

Flash sintering of alumina require higher electric field (>1000 V cm^{-1}). However, addition of impurities modifies the onset of flash sintering, both in terms of applied field and also by reducing the sintering temperature. The doped alumina shows flash sintering at 1000 V cm^{-1}, while un-doped alumina require higher applied field. Similarly the different dopant have different onset for flash sintering. The MgO doped alumina sinters at lower temperature then Fe$_2$O$_3$ doped alumina for a same applied field. As MgO was well known for its ability to segregate on the grain boundary, Whereas Fe$_2$O$_3$ has very high solubility at higher temperature.

Chapter 5
Conclusions and future outlook

5.1 Conclusions

A newly born flash sintering or field assisted technique for sintering of ceramics has been presented in this thesis. The proposed research activity describes the flash sintering procedure to sinter alumina zirconia composite, hydroxyapatite and even insulating un-doped and doped alumina.

In case of alumina-zirconia composite the flash effect is shown to occur at the same applied electric field as that of 3YSZ. However, for semiconducting hydroxyapatite and insulating alumina the field strength required to induce flash effect is much higher in contrast with 3YSZ. For 3YSZ electric field effect is known to occur in two distinct mechanisms FAST and flash, whereas in composite the sintering comprises of FAST in the initial stage and then transitions into flash mode.

The phenomena of flash sintering occur in three different stages. In stage I, sintering process is similar to that of FAST sintering. When transition occurs from semiconducting to conducting, it can be defined as stage II, which is controlled by the power supply by switching voltage to current control. In current control mode voltage decreases and then remains constant, which is stage III.

Grain growth in free sintering is more pronounced in the final stage of sintering. Similarly, in flash sintering, if specimen attained

higher density in stage II then grain growth will occur in the stage III of flash sintering. The grain size can be controlled by controlling current density and the post flash time. It is also observed that grain size decreases with increase in the applied electric field.

The characteristic effect of nucleation and growth is observed under isothermal flash sintering experiments. The flash is seen to occur with an incubation time, and it depends on the furnace temperature and applied electric field. Based on the isothermal experiments a model for nucleation and growth of embryo is presented. The nucleation is proposed to occur at the furnace temperature, and joule heating is observed during post flash sintering. Therefore nucleation is the precursor to the onset of flash and Joule heating is a consequence of nucleation process.

The flash sintering is even observed in proton conducting hydroxyapatite. However, it requires higher field range of 1000 V cm^{-1} to 2000 V cm^{-1}. The sintered samples are shown to densify to a relative density > 90 % by flash sintering technique. At high temperature and low applied field, flash sintering leads to c-axis growth of HA crystal.

The addition of impurity decrease the magnitude of field and threshold temperature for flash, but concentration of impurities does not induce much influence on the onset of flash sintering.

5.2 Future outlook

More accurate measurement of specimen temperature is required to calculate the actual specimen temperature during flash sintering. The common procedure used for measuring specimen temperature was by pyrometric measurement during flash sintering. However pyrometer can measure the surface temperature and not

the bulk temperature, which could be much higher than the temperature observed during sintering.

Experiments reported shown the grain growth with respect to current density or post flash stage. Similarly it will be also interesting to measure grain size involving same flash condition with increased furnace temperature.

Results presented suggest influence of grain boundary properties on flash sintering. This could be analysed in more detail with the help of dielectric measurement on a two phase system. Even some high resolution TEM analysis will be helpful to analyse this interesting effect of flash sintering.

Flash sintering of hydroxyapatite needs to be analysed in much more detailed way with respect to current density. Even higher density can be achieved by controlling the current density. Additionally, grain growth analysis of hydroxyapatite will be much more helpful in obtaining fine grain microstructure. Flash sintering temperature of HA can be lower by carrying out isothermal flash sintering experiments at much lower temperature. Also it could be interesting to observe nanometric particle effect on flash sintering of hydroxyapatite. It remains to analyse the micrograph of flash sintered un-doped and doped alumina.

The initiation of a flash event has the signature of the nucleation but the post flash events involve many complex phenomena, which need further detailed investigations through both experiments and modelling.

References:

[1]   Chiang Yet-Ming, P. Dunbar, W. D. K. Birnie, Physical
        Ceramics: Principles for Ceramic Science and Engineering.
        1997, John Wiley & Sons, USA.

[2]   Cologna, M., B. Rashkova, R. Raj, Flash Sintering of
        Nanograin Zirconia in <5 s at 850°C. J Am Ceram Soc, 2010.
        93: p. 3556–9.

[3]   Cologna, M., A.L.G. Prette, R. Raj, Flash-Sintering of Cubic
        Yttria-Stabilized Zirconia at 750°C for Possible Use in SOFC
        Manufacturing. J Am Ceram Soc, 2011. 94: p. 316–9.

[4]   Francis, J. S. C., R. Raj, Flash-Sinterforging of Nanograin
        Zirconia: Field Assisted Sintering and Superplasticity. J Am
        Ceram Soc, 2012. 95: p. 138–46.

[5]   Francis, J. S. C., R. Raj, Influence of the Field and the
        Current Limit on Flash Sintering at Isothermal Furnace
        Temperatures. J Am Ceram Soc, 2013. 96: p. 2754–8.

[6]   M'Peko, J-C., J. S. C. Francis, R. Raj, Impedance
        Spectroscopy and Dielectric Properties of Flash Versus
        Conventionally Sintered Yttria-Doped Zirconia
        Electroceramics Viewed at the Microstructural Level. J Am
        Ceram Soc, 2013. 96(12): p. 3760-7.

[7]   Steil, M. C., D. Marinha, Y. Aman, J. R. C. Gomes, M. Kleitz,
        From conventional ac flash-sintering of YSZ to hyper-flash
        and double flash. J Eur Ceram Soc, 2013. 33: p. 2093–101.

[8]   Baik, S., J. Moon, Effects of Magnesium Oxide on Grain-
        Boundary Segregation of Calcium During Sintering of
        Alumina. J Am Ceram Soc, 1991. 22: p. 819–22.

[9]   Cologna, M., J. S. C. Francis, R. Raj, Field assisted and flash sintering of alumina and its relationship to conductivity and MgO-doping. J Eur Ceram Soc, 2011. 31: p. 2827–37.

[10]   Miyayama, M., H. Yanagida, A. Asada, Effects of Al2O3 additions on resistivity and microstructure of yttria-stabilized zirconia. Am Ceram Soc Bull, 1985. 65(4): p. 660–4.

[11]   Navarro, L.M., P. Recio, J. R. Jurado, P. Duran, Preparation and properties evaluation of zirconia-based / AI203 composites as electrolytes for solid oxide fuel cell systems Part III Mechanical and electrical characterization, J Mater Sci, 1995. 30: p. 1949–60.

[12]   Yuzaki, A. and A. Kishimoto, Effect of Alumina Dispersion on Ionic Conduction of Toughened Zirconia Base Composite. Solid State Ionics, 1999. 116: p. 47-51.

[13]   Kumar, B., J. S. Thokchom, Space Charge-Mediated Ionic Transport in Yttria-Stabilized Zirconia–Alumina Composite Membranes. J Am Ceram Soc, 2008. 91: p. 1175–81.

[14]   Guo, X., R. Waser, Electrical properties of the grain boundaries of oxygen ion conductors: Acceptor-doped zirconia and ceria. Prog Mater Sci, 2006. 51: p.151–210.

[15]   Verkerk, M. J., B. J. Middelhuis and A. J. Burggraaf, Effect of grain boundaries on the conductivity of high-purity ZrO2-Y203 ceramics. Solid State Ionics, 1982. 6: p. 159–70.

[16]   Lange, F., M. Hirlinger, Hindrance of Grain Growth in Al2O3 by ZrO2 Inclusions. J Am Ceram Soc, 1984. 67: p. 164–8.

[17]   Hori, S., R. Kurita, M. Yoshimura, S. Sōmiya, Suppressed grain growth in final-stage sintering of Al_2O_3 with dispersed ZrO 2 particles. J Mater Sci Lett, 1985. 4: p. 1067–70.

[18]   Oonishi, H. Orthopaedic applications of hydroxyapatite. Biomaterials, 1991. 12: p. 171–8.

[19]   Zyman, Z., V. Glushko, V. Filippenko, V. Radchenko, V. Mezentsev, Nonstoichiometric hydroxyapatite granules for orthopaedic applications. J Mater Sci Mater Med, 2004. 15: p. 551–8.

[20]   Schwartz, C., P. Lecestre, P. Frayssinet, P. Liss, Orthopaedic Surgery & Bone substitutes. Eur J Orthop Surg Traumatol, 1999. 9: p. 161–5.

[21]   Kalita, S. J., A. Bhardwaj, H. Bhatt, Nanocrystalline calcium phosphate ceramics in biomedical engineering. Mater Sci Eng C, 2007. 27: p. 441–9.

[22]   Muralithran, G., S. Ramesh, The effects of sintering temperature on the properties of hydroxyapatite. Ceram Int, 2000. 26: p. 221–30.

[23]   Raynaud, S., E. Champion, J. P. Lafon, D. Bernache-Assollant, Calcium phosphate apatites with variable Ca/P atomic ratio III. Mechanical properties and degradation in solution of hot pressed ceramics. Biomaterials, 2002. 23: p. 1081–9.

[24]   Veljović, D., B. Jokić, R. Petrović, E. Palcevskis, A. Dindune, I. N. Mihailescu, Processing of dense nanostructured HAP ceramics by sintering and hot pressing. Ceram Int, 2009. 35: p. 1407–13.

[25]   Wakai, F., Y. Kodama, S. Sakaguchi, T. Nonami, Superplasticity of Hot Isostatically Pressed Hydroxyapatite. J Am Ceram Soc, 1990. 73: p. 457–60.

[26]   Fang, Y., D. K. Agrawal, D. M. Roy, R. Roy, Microwave sintering of hydroxyapatite ceramics. J Mater Res, 2011. 9: p. 180–7.

[27]   Yang, Y., J. Ong, J. Tian, Rapid sintering of hydroxyapatite by microwave processing. J Mater Sci Lett, 2002. 21: p. 67–9.

[28]   Gu, Y. W., N. H. Loh, K. Kho, S. B. Tor, P. Cheang, Spark
        plasma sintering of hydroxyapatite powders. Biomaterials,
        2002. 23: p. 37–43.

[29]   Champion, E., Sintering of calcium phosphate bioceramics.
        Acta Biomater, 2013. 9: p. 5855–75.

[30]   Kang, S-J. Sintering. 2004, Elsevier Butterworth-Heinemann.
        p. 3-4.

[31]   Castro, R. H. R. and K. V. Benthem, Sintering. 2013, Spring-
        er-Verlag Berlin Heidelberg.

[32]   Mohamed N. Rahaman. Sintering of Ceramics. 2008, Marcel
        Dekker, Inc.

[33]   Coble, R. L., Sintering Crystalline Solids. I. Intermediate and
        Final State Diffusion Models. J Appl Phys, 1961. 32: p. 787–
        92.

[34]   Kang, S-J, Sintering. 2004, Elsevier Butterworth-Heinemann.

[35]   Shen, Z., M. Johnsson, Z. Zhao, M. Nygren, Spark Plasma
        Sintering of Alumina. J Am Ceram Soc, 2002. 27: p. 1921–7.

[36]   Hungría, T., J. Galy, A. Castro, Spark Plasma Sintering as a
        Useful Technique to the Nanostructuration of Piezo-
        Ferroelectric Materials. Adv Eng Mater, 2009. 11: p. 615–31.

[37]   Miao, X., Y. Chen, H. Guo, K. A. Khor, Spark plasma sintered
        hydroxyapatite-yttria stabilized zirconia composites. Ceram
        Int, 2004. 30: p. 1793–6.

[38]   Alvarez-Clemares, I., G. Mata-Osoro, A. Fernández, S.
        Lopez-Esteban, C. Pecharroman, R. Torrecillas, Ceria doped
        alumina by Spark Plasma Sintering for optical applications. J
        Eur Ceram Soc, 2012. 32: p. 2917–24.

[39]   Prette, A. L. G., M. Cologna, V. Sglavo, R. Raj, Flash-
        sintering of Co2MnO4 spinel for solid oxide fuel cell
        applications. J Power Sources, 2011. 196: p. 2061–5.

[40]   Gaur, A., V. M. Sglavo, Flash-sintering of MnCo2O4 and its relation to phase stability. J Eur Ceram Soc, 2014 34(10): p. 2391-2400.

[41]   Gaur, A., V. M. Sglavo, Densification of $La_{0.6}Sr_{0.4}Co_{0.2}Fe_{0.8}O_3$ ceramic by flash sintering at temperature less than 100°C. J Mater Sci, 2014. 49: p. 6321-32.

[42]   Downs, J. A., V. M. Sglavo, Electric Field Assisted Sintering of Cubic Zirconia at 390°C. J Am Ceram Soc, 2013. 96: p. 1342–4.

[43]   Jha, S., R. Raj, The Effect of Electric Field on Sintering and Electrical Conductivity of Titania. J Am Ceram Soc, 2013. 97(2): p. 527-34.

[44]   Karakuscu, A., M. Cologna, D. Yarotski, J. Won, J. S. C. Francis, R. Raj, Defect Structure of Flash-Sintered Strontium Titanate. J Am Ceram Soc, 2012. 95: p. 2531–6.

[45]   Yoshida, H., Y. Sakka, T. Yamamoto, J-M. Lebrun, R. Raj, Densification behaviour and microstructural development in undoped yttria prepared by flash-sintering. J Eur Ceram Soc, 2014. 34: p. 991–1000.

[46]   Raj, R., Joule heating during flash-sintering. J Eur Ceram Soc, 2012. 32: p. 2293–301.

[47]   Francis, J. S. C., A study on the phenomena of flash-sintering with tetragonal zirconia. PhD Thesis, 2013.

[48]   Raj, R., M. Cologna, J. S. C. Francis, Influence of Externally Imposed and Internally Generated Electrical Fields on Grain Growth, Diffusional Creep, Sintering and Related Phenomena in Ceramics. J Am Ceram Soc, 2011. 94: p. 1941–65.

[49]   Baraki, R., S. Schwarz, O. Guillon, Effect of Electrical Field/Current on Sintering of Fully Stabilized Zirconia. J Am Ceram Soc, 2012. 95: p. 75–8.

[50]   Francis, J. S. C., M. Cologna, R. Raj, Particle size effects in flash sintering. J Eur Ceram Soc, 2012. 32: p. 3129–36.

[51]   Narayan, J., A new mechanism for field-assisted processing and flash sintering of materials. Scr Mater, 2013. 69: p. 107–11.

[52]   Pure Alumina, TAIMEI CHEMICALS CO. L. Taimicron 2011.

[53]   3 mol% yttria stabilised zirconia, Tosoh zirconia powder 2004.

[54]   Hydroxyapatite Datasheet, Technical Datasheet nanoXIM □ HAp201: p. 2–4.

[55]   Company R and H. DURAMAX^{TM} B-1000 Binder 2008.

[56]   Venkatachari, K., R. Raj, Shear deformation and densification of powder compacts. J Am Ceram Soc, 1986. 69: p. 499–506.

[57]   Rhee, Y., H. Lee, S. Kang, Diffusion induced grain-boundary migration and mechanical property improvement in Fe-doped alumina. J Eur Ceram Soc, 2003. 23: p. 1667–74.

[58]   Naik, K. S., V. M. Sglavo and R. Raj, Field assisted sintering of ceramic constituted by alumina and yttria stabilized zirconia. J Eur Ceram Soc, 2014. 34(10): p. 2435–42.

[59]   Mendelson, M., Average grain size in polycrystalline ceramics. J Am Ceram Soc, 1969. 52: p. 443–6.

[60]   Wurst, J., J. Nelson, Lineal Intercept Technique for Measuring Grain Size in Two Phase Polycrystalline Ceramics. J Am Ceram Soc, 1972. 46: p. 109.

[61]   Richard, E. C., Ceramography. Preparation and Analysis of Ceramic Microstructures. 2006, John Wiley & Sons, Inc.

[62]   Alaruri, S., L. Bianchini, A. Brewington, Effective spectral emissivity measurements of superalloys and YSZ thermal barrier coating at high temperatures using a 1.6μm single wavelength pyrometer. Opt Lasers Eng, 1998. 30: p. 77–91.

[63]   Ghosh, S., A. H. Chokshi, P. Lee, R. Raj, A Huge Effect of Weak dc Electrical Fields on Grain Growth in Zirconia. J Am Ceram Soc, 2009. 92: p. 1856–9.

[64]   Yang, D., R. Raj, H. Conrad, Enhanced Sintering Rate of Zirconia (3Y-TZP) Through the Effect of a Weak dc Electric Field on Grain Growth. J Am Ceram Soc, 2010. 93: p. 2935–7.

[65]   Burke, J. E., D. Turnbull, Recrystallization and grain growth. Prog Met Phys, 1952. 3: p. 220–92.

[66]   Hillert, M., On the theory of normal and abnormal grain growth. Acta Metall, 1965. 13: p. 227–38.

[67]   Simmons, J., Poole-Frenkel Effect and Schottky Effect in Metal-Insulator-Metal Systems. Phys Rev, 1967. 155: p. 657–60.

[68]   Thomson, J., [Letters to Editor] 1910. 83: p. 460–460.

[69]   Fisher, J. C., J. H. Hollomon, D. Turnbull, Nucleation. J Appl Phys, 1948. 19: p. 775.

[70]   Turnbull, D., Transient nucleation. Met Technol, 1948. p. 15.

[71]   Guillemet-Fritsch, S., Z. Valdez-Nava, C. Tenailleau, T. Lebey, B. Durand, J-Y. Chane-Ching, Colossal Permittivity in Ultrafine Grain Size $BaTiO_{3-x}$ and $Ba_{0.95}La_{0.05}TiO_{3-x}$ Materials. Adv Mater, 2008. 20: p. 551–5.

[72]   Hu, W., Y. Liu, R. L. Withers, T. J. Frankcombe, L. Norén, A. Snashall, Electron-pinned defect-dipoles for high-performance colossal permittivity materials. Nat Mater 2013. 12: p. 821–6.

[73]   Han, H., D. Ghosh, J. L. Jones, J. C. Nino, Colossal
        Permittivity in Microwave-Sintered Barium Titanate and Effect
        of Annealing on Dielectric Properties. J Am Ceram Soc,
        2012. 96(2): p. 485-90.

[74]   Arlt, G., D. Hennings, Dielectric properties of fine-grained
        barium titanate ceramics. J Appl Phys, 1985. 58: p. 1619-25.

[75]   Zunger A., University of Colorado at Boulder, private
        communication.

[76]   Guo, X., Roles of alumina in zirconia for functional
        applications. J Am Ceram Soc, 2003. 86: p. 1867–73.

[77]   Grossin, D., S. Rollin-Martinet, C. Estournès, F. Rossignol, E.
        Champion, C. Combes, Biomimetic apatite sintered at very
        low temperature by spark plasma sintering: physico-
        chemistry and microstructure aspects. Acta Biomater, 2010.
        6: p. 577–85.

[78]   Horiuchi, N., M. Nakamura, A. Nagai, K. Katayama, K.
        Yamashita, Proton conduction related electrical dipole and
        space charge polarization in hydroxyapatite. J Appl Phys,
        2012. 112: p. 074901(1-6).

[79]   Kimihiro, Y., K. T. U. Kitagaki, Thermal instability and proton
        conductivity of ceramic hydroxyapatite at high temperatures.
        J Am Ceram Soc, 1995. 78: p. 1191–7.

[80]   Akazawa, H., Y. Ueno, Growth of preferentially c-axis
        oriented hydroxyapatite thin films on Si(100) substrate by
        electron-cyclotron-resonance plasma sputtering. Appl Surf
        Sci, 2013. 276: p. 217–22.

Curriculum Vitae

Educational background

PhD.

Department of Materials Science and Industrial Engineering, University of Trento, Trento, Italy (2011-2014)

Master of Science
Department of Chemistry, Goa University, India (2008-2010)

Bachelor of Science
D.M.'s college, Goa, India (2005-2008)

Research Experience

International Mobility program:
Department of Mechanical Engineering, University of Colorado at Boulder, CO, Boulder, USA. (September 2012- December 2012)

Master's Thesis:
Synthesis and characterization of $Ni_x Mg_{(1-x)} Fe2O4$

Undergraduate thesis:
Synthesis and Conductivity studies of Polyarylamines

Publications and Proceedings

Naik, K.S., Sglavo, V.M., and Raj, R., *"Field assisted sintering of ceramic constituted by alumina and yttria stabilized zirconia".* Journal of the European Ceramic Society, 2014; 34; 2435–2442.

Naik, K.S., Sglavo, V.M., and Raj, R., *"Flash sintering as a nucleation phenomenon and a model thereof"*. Journal of European Ceramic Society, 2014. DOI: 10.1016/j.jeurceramsoc.2014.04.043

Downs, J.A., **Naik, K.,** Anshu, Sglavo, V.M. "Electric Field Assisted Sintering in Advanced Ceramics". *Proceedings of the XI Convegno Nazionale AIMAT* (2012)

Conferences/Symposiums

Naik, K.S., Raj, R., Sglavo, V.M. "Flash sintering of YSZ-alumina composite" at 13th European Ceramic Society conference 2013, Limoges (France)

Naik, K.S., Downs, J.A., Sglavo, V.M. "Effect of dopant on flash sintering behaviour of alumina" at Materials Science & Technology Symposium 2012 Pittsburgh, Pennsylvania (USA)

Panjikar, P.C., **Naik, K.S.,** Patil, S., Harmalkar, V., Desai, V.G. "Conductivity studies of Polyarylamines" at a symposium on fascinating world of chemical sciences held at Goa University, 2008, Goa (India)

Acknowledgements

First and foremost I would like to express my sincerest gratitude to my supervisor, Prof. Vincenzo Maria Sglavo, whose encouragement, guidance and support throughout the period of my Ph.D. enabled me to develop an understanding of the subject. I have been amazingly fortunate to have him as an advisor who gave me the freedom and opportunity to explore.

I am deeply grateful to Prof. Rishi Raj for giving me a chance to work as a part of his research group during my mobility program at UCB Boulder. His continuous suggestion always helped me to improve my scientific knowledge and experimental skills.

I would like to thanks Dr. John Downs and Dr. Marco Cologna for their initial help with experimentation and all time suggestion throughout the PhD.

I would like to express my sincere thanks to Dr. John Francis and Mr. Shikhar Jha for their help and consideration during my stay in Boulder. I thank Alex Iselin and John Burkhardt for making my life comfortable in boulder.

Many of my friends have helped me through these years: I especially thank Rohan, Pradeep, Pradnyesh, Pranay, Anshu, Rahul, Lam, Pushkar, Piyush and all my trendians friends for making my stay memorable with lots of fun. I thank all my close friends and teachers in India for being there for me. I will keep on record my sincere thanks to all the Professors and colleagues in Ceramic laboratory for all their help and support during my stay.

Most important, none of this would have been possible without the love and patience of my family and my grandparents who are no longer here, but always been the most influential people in my life.